Hughes, A., Rood, D.H., DeVecchio, D.E., Whittaker, A.C., Bell, R.E., Wilcken, K.M., Corbett, L.B., Bierman, P.R., Swanson, B.J., and Rockwell, T.K., 2021, Tectonic controls on Quaternary landscape evolution in the Ventura basin, southern California, USA, quantified using cosmogenic isotopes and topographic analyses: GSA Bulletin, https://doi.org/10.1130/B36076.1.

Supplemental Material

Figure S1. Balanced cross sections through the Long Canyon syncline taken from Huftile and Yeats (1996). The dip-slip offsets, which are included in Table 1, were calculated in Huftile and Yeats (1996) by retro-deforming these balanced cross sections. (A) Present day. (B) Retro-deformed to the top of the exposed Saugus Formation. (C) Retro-deformed to the base of the Las Posas Formation. Ages in boxes refer to the isochron burial ages for the appropriate horizon and the age in brackets below refers to the age interpretation for the same horizon in Huftile and Yeats (1996). Line of section is included on Figure 1.

Figure S2. Log-gradient as a function of log-drainage area for the study area. The plot on the left is for all streams with upstream drainage area >50,000 m^2, which indicates a threshold drainage area of 10^6 m^2. However, using a threshold drainage area of 10^6 m^2 results in stream heads that are not consistent with stream heads visible in the 10 m^2 digital elevation model. The plot on the right is for all stream segments shown in figure 8A with drainage area >0.5×10^6 m^2. The slope of 0.48 ± 0.0004 (error is one standard error) in the plot on the right is used to justify our reference concavity of 0.50.

Figure S3. A plot of ^{26}Al-^{10}Be concentrations (gray circles) for the burial dating samples collected from the top of the exposed Saugus Formation in the hanging wall of the Southern San Cayetano fault. Error bars are 1σ. Several of the samples are indistinguishable from the surface production ratio (dashed black line), which indicates that these samples may be too young for ^{26}Al/^{10}Be isochron burial dating.

Figure S4. (A) Geological map showing the location of isochron burial dating samples (stars) in the eastern Ventura basin. Mapped geological units are from Campbell et al. (2014). The colored circles represent the locations of paleomagnetic samples, which along with the location of the ash layer (dashed line with v's), are taken from Levi and Yeats (1993). Map location is shown on Figure 1. (B) Interpretation of the magnetic samples from Levi and Yeats (1993) based on the correlation of the ash layer in the Saugus Formation with the 0.76 Ma Bishop Ash.

Figure S5. Landslides in the hanging wall of the eastern section of the San Cayetano fault triggered by the 1994 M 6.7 Northridge earthquake. Landslides originally mapped by Harp and Jibson (1995) and recently amended by Townsend et al. (2020). Northridge earthquake landslides cover 2% of the surface area of catchment 9 and 5% of the surface area of catchment 10. Grid coordinates are in Universal Transverse Mercator (zone 11S).

Figure S6. Photos showing large boulders in Sisar Creek (catchment 5). Boulders occasionally in excess of 2 m tall may armor the channel, decrease channel incision, and, therefore, decrease erosion rates measured from channel sands. Photo locations: (A) Lat: 34° 27′ 16.662" N, Lon: 119° 8′ 2.93" W; (B) Lat: 34° 27′ 44.502" N, Lon: 119° 7′ 49.94" W; (C) Lat: 34° 27′ 16.62" N, Lon: 119° 8′ 2.88" W; (D) Lat: 34° 27′ 52.482" N, Lon: 119° 7′ 48.99" W. Photos provided by Brian Swanson.

Table S1. Sensitivity analysis addressing the incorporation of uncertainty in the $^{26}Al/^{10}Be$ surface production ratio into the burial ages

Table S2. Full sample parameters for isochron burial dating samples

Table S3. Sample parameters for the surface exposure dating samples from the Bear Canyon surface

Table S4. Parameters for ^{10}Be erosion rate samples and inputs to CRONUS calculator

Table S5. Well data for wells used in cross section in Figure 6B

Table S6. Alternative isochron burial ages

Table S7. Details on process blanks for ^{10}Be analysis

Table S8. Details on process blanks for ^{26}Al analysis

Table S9. ^{10}Be details for CRONUS-N samples

Table S10. ^{26}Al details for CRONUS-N samples

1. COSMOGENIC NUCLIDE MEASUREMENT TECHNIQUES: BACKGROUND, SAMPLING METHODS, AND DATA REDUCTION

This study incorporates ^{26}Al–^{10}Be isochron burial dating, cosmogenic ^{10}Be-derived erosion rates, and ^{10}Be surface exposure dating. All three techniques are based on the same basic physics where rocks and soils near the Earth's surface accumulate terrestrial cosmogenic nuclides (TCN) primarily by nuclear spallation reactions via the interaction of cosmic rays from space with minerals contained in rocks or soils (Lal, 1991; Lal and Peters, 1967). In this study, we focus on the nuclides ^{10}Be and ^{26}Al, which are formed by the interaction of cosmic ray-derived secondary particles with O and Si in quartz (Lal, 1988). The penetration of cosmogenic ray-derived secondary neutrons, and the production rate of spallation-induced cosmogenic nuclides, decreases exponentially with depth to ~2–3 m below the surface (depending on material density). Therefore, the concentration of cosmogenic nuclides in a sample should reflect the time the sample has spent within the zone of nuclide production. Using this basic theory, different sampling strategies and methods of data reduction can be applied to calculate burial ages, exposure ages, or to quantify rates of erosion.

1.1 Isochron burial dating on the Saugus Formation: background

Isochron burial dating is a key tool for dating Quaternary sediments and can be applied to a wide range of terrestrial and marine deposits (e.g., Balco and Rovey, 2008; Balco et al., 2013; Bender et al., 2016; Çiner et al., 2015; Erlanger et al., 2012). Once a deposit is buried below the penetration depth of cosmic rays, cosmogenic nuclide production will cease and the nuclide concentration becomes primarily a function of radioactive decay, which occurs at a rate dependent on the radioactive half-life of the specific cosmogenic nuclide. The currently-accepted value for the half-life of ^{10}Be is measured at $1.387 +/- 0.012 \times 10^6$ yr^{-1} (Chmeleff et al., 2010) and for ^{26}Al the half-life is $0.708 +/- 0.017 \times 10^6$ yr^{-1} (Nishiizumi, 2004). The respective half-lives of ^{10}Be and ^{26}Al define an ideal age range for cosmogenic isotope isochron burial dating between ~0.2–5 Ma, although this range is dependent upon initial nuclide concentrations within the samples prior to deposition. The Saugus Formation is an ideal target for isochron burial dating because the estimated age is between 0.2 and 2.3 Ma (Levi and Yeats, 1993; Wehmiller et al., 1978). Additionally, the provenance for much of the Saugus Formation is the San Gabriel Mountains or the Topatopa Mountains (Fig. 1) (Levi and Yeats, 1993; Heirshberg, 1997), which is composed of igneous and metamorphic rocks or Tertiary sandstones, respectively. These source rocks provide abundant quartz required for the measurement of ^{10}Be and ^{26}Al (Campbell et al., 2014).

Simple burial dating assumes minimal post-burial production has affected a single sample, which limits the application to very specific settings such as cave deposits (Granger and Muzikar, 2001). The advantage of the isochron burial dating method is that a suite of multiple samples with the same burial age, but varying pre-depositional exposure and erosion histories, can be analyzed simultaneously (Balco and Rovey, 2008). Several assumptions are required to use isochron burial dating. Firstly, the period of exposure during transport and prior to deposition in the current deposit should be short enough that no significant radioactive decay occurred during transportation. The ~3600 m thick succession of Saugus Formation sediments within the central Ventura basin, all of which are thought to be Pleistocene in age, suggests high sedimentation rates and associated rapid erosion rates (Yeats, 1988). High sedimentation rates

suggest that the Saugus Formation was transported and deposited rapidly, and that minimal decay will have occurred prior to deposition.

A second assumption is that all clasts should share the same post-burial history and, therefore, post-burial nuclide production can be treated as a constant among a suite of samples. To address this, samples for burial dating of the Saugus Formation were collected from the same depth horizon (within +/– 30 cm). Sampling from the same depth horizon also increases the chances that, although all clasts likely have different prior depositional and erosional histories, they should all share the same post-burial history. Additionally, samples must have been rapidly buried to a depth below the cosmogenic nuclide production zone to ensure that post-burial production by neutron spallation does not overprint the signal of post-burial decay. We sampled from a depth of > 2 m from the surface to increase the probability that post-burial production by neutron spallation does not overprint the decay signal (Balco and Rovey, 2008).

For each isochron, the goal was to collect around eight individual cobble-sized samples, an amalgamated sample of approximately fifty pebble-sized clasts, and a bulk sample (~2 kg) of sand. The aim of sampling this range of grain sizes is to capture a wide range of erosional processes which should increase the chance of sampling from clasts with a variety of nuclide concentrations to plot on an isochron. Unweathered quartz-rich cobbles and pebbles were selected to maximize the amount of target mineral for ^{10}Be and ^{26}Al analyses, and samples were collected from within the same stratigraphic unit to ensure a similar shared burial history across the individual samples at a specific sampling location.

Isochrons and associated ages were plotted using a Bayesian linear regression approach (Bender et al., 2016). The Bayesian approach resolves a correlation between slope and intercept for numerous different regressions within a predefined set of errors in x–y data (i.e., ^{10}Be–^{26}Al concentration space). For burial dating isochrons, the maximum slope of the regression is set at 6.75, to be consistent with the standard surface production ratio of ^{26}Al/^{10}Be of 6.75 (Balco and Rovey, 2008). The minimum slope is zero. The likelihood of each regression of slope and intercept is recorded in normalized probability histograms, which also illustrate whether the set of regressions represents a Gaussian distribution. The calculations were performed with a Matlab script that runs Monte Carlo simulations to conduct 1,000,000 trial runs to calculate slope and intercept values from ^{10}Be and ^{26}Al concentrations and associated 1σ measurement errors (Bender et al., 2016). The Matlab script also calculates the likelihood of each slope and intercept value, assuming a Gaussian distribution (Bender et al., 2016). Output values for most likely estimate of slope (the modal value) are input into Equation 1 of the main manuscript to calculate the burial age. Uncertainties are plotted by inputting 95% confidence values into Equation 1 from the main manuscript.

1.2 Isochron burial sample locations

We sampled the base of the Las Posas Formation in the hanging wall of the Ventura fault from a bed of pebbles and cobbles in a road cut exposure in Hall Canyon, immediately above what we identified in the field as the transition from the Las Posas Formation to the underlying Mudpit Claystone member of the Pico Formation. However, the contact is gradational so the samples may be located several meters above or below the mapped contact. Samples to date the top of the exposed Saugus Formation at Ventura were located ~50 m below the top of the mapped extent of the Saugus Formation in a track-cut exposure located just behind Ventura City Hall, on the south limb of the Ventura Avenue Anticline (Dibblee and Ehrenspeck., 1988).

We collected samples to date the Grimes Canyon deltaic facies, which underlies the Saugus and Las Posas Formations in the hanging wall of the Oak Ridge fault (Fig. 2), from a road cut exposure along State Route 23 where the Grimes Canyon deltaic facies interfingers with Pico Formation ~50 m up section from the base of the Grimes Canyon deltaic facies (Figs. 2 and 6; Campbell et al., 2014). We obtained samples to date the top of the exposed Saugus Formation in the hanging wall of the Oak Ridge fault from the axis of the Long Canyon syncline (Fig. 6). We collected the Long Canyon syncline samples from a stream-cut exposure located as close as possible to what is mapped as the core of the syncline (Fig. 6B). The goal was to sample the youngest preserved sediments that, in theory, should be preserved in the core of the syncline. Samples from the core of the Happy Camp syncline were collected from a track-cut exposure located within sediments mapped as either the terrestrial Saugus Formation (Dibblee and Ehrenspeck, 1992) or tentatively within the Grimes Canyon deltaic facies (Campbell et al., 2014).

In the eastern Ventura basin, we collected samples to date the top of the exposed Saugus Formation at the mapped location of the contact between the Saugus Formation and overlying upper Saugus Formation (Fig. S4; Campbell et al., 2014). We obtained samples to date the base of the brackish water Sunshine Ranch member of the Saugus Formation from a channelized pebble and cobble horizon within a large road-cut exposure at the end of the south bound off-ramp from the I-5 freeway to Calgrove Boulevard. The sample was located ~10 m stratigraphically above the contact with marine sediments mapped as part of the upper Pico Formation (Figure S4; Campbell et al., 2014). We note, however, that field observations indicate that deposits at the sample location more closely resemble terrestrial Saugus deposits rather than shallow marine or brackish deposits.

1.3 Exposure dating using boulder sampling; background, sampling strategy, and data reduction

Terrestrial cosmogenic nuclide (TCN) exposure dating for surface clasts, including boulders, is a well-established technique for dating various Pleistocene sedimentary landforms such as glacial surfaces (e.g., Rood et al., 2011; Wesnousky et al., 2016) or alluvial fans (e.g., Behr et al., 2010; Frankel et al., 2007; Owen et al., 2014). Post-depositional exhumation of a clast from the subsurface by the erosion of surrounding material can affect the measured nuclide concentration within a boulder and, consequently, the apparent age. Specifically, if a boulder has been exhumed, then the production rate will have varied through time as the amount of shielding from the surrounding soils decreased. Consequently, an exhumed boulder will give an apparent age that will underestimate the true age for the deposit or surface (Behr et al., 2010; Heyman et al., 2016; Rood et al., 2011). Significant erosion of the outer surface of a boulder can reduce measured nuclide concentrations relative to if the boulder was uneroded and will also result in apparent exposure ages that underestimate the exposure age (DeVecchio et al., 2012b; Rood et al., 2011). In contrast, a large inherited nuclide concentration can artificially increase the apparent exposure age of the boulder surface.

We sampled the upper 2–5 cm of the tops of each boulder and from the center of flat topped boulders to reduce the effects of fire spallation (Bierman and Gillespie, 1991) and uncertainties relating to surface geometry (Nishiizumi et al., 1989). Where possible, care was taken to avoid sampling anomalously fresh, unweathered boulder surfaces, which may indicate recent breakage of the boulder. We also selected boulders with case-hardening, polishing, and

low surface relief because these characteristics indicate that the boulder has undergone minimal erosion of the outer surface. The latitude, longitude, and elevation of each boulder was measured using a handheld GPS and topographic shielding was measured at each boulder using a clinometer and compass.

^{10}Be exposure ages were calculated using version 3.0 of the CRONUS-Earth online exposure age calculator (Balco et al., 2008). Topographic shielding corrections were made using the CRONUS-Earth online geometric shielding calculator, version 2 (available at: http://stoneage.ice-d.org/math/skyline/skyline_in.html). We employed a reference production rate for ^{10}Be of 4.22 +/– 0.16 atoms g^{-1} based on the Promontory Point (PPT) reference production rate calibration data from Lake Bonneville, Utah, USA (Lifton et al., 2015) and used the production rate scaling scheme of Lal (1991) and Stone (2000).

The exposure age for the uplifted Bear Canyon alluvial fan surface is based on the average exposure age for the three oldest boulders assuming that the remaining seven samples have been exhumed by erosion of alluvial fan surface material surrounding the boulders since their time of deposition (Fig. 7). If boulders are exhumed after deposition, then all nuclides that would have accumulated at the surface from the time of deposition to the time of exhumation are not necessarily accounted for, and measured ^{10}Be concentration will be lower than the ^{10}Be concentration that reflects the true exposure age of the surface (Behr et al., 2010; Heyman et al., 2016). Therefore, our preferred exposure age of 121.2 +/- 11.6 ka is based on the three oldest boulders and assumes that the boulders below 2.4 m height have been exhumed since initial deposition and the ^{10}Be concentration in the boulders below 2.4 m height does not reflect the true exposure age of the surface.

1.4 ^{10}Be catchment-averaged erosion rates; background and sampling

Bedrock in an actively eroding landscape accumulates cosmogenic nuclides (including ^{10}Be) as it passes upwards through the production zone of cosmogenic nuclides before being weathered and eroded from the hillslope as regolith, transported, and deposited as sediment in an active channel. In eroding landscapes, where both nuclide production during transportation and radioactive decay can be ignored and sediment is well mixed, the concentration of ^{10}Be within a sand sample from an active fluvial channel is proportional to the catchment-averaged ^{10}Be production rate and is inversely proportional to the spatially averaged erosion rate (Bierman and Steig, 1996; Granger et al., 1996; Lal, 1991). Consequently, rapidly eroding catchments will have low nuclide concentrations and slowly eroding catchments will have high nuclide concentrations.

The relationship between nuclide concentration and spatially-averaged erosion rates depends upon an approximately uniform and evenly distributed upstream percentage of quartz to ensure that the supply of quartz to the catchment is evenly sourced (Bierman and Steig, 1996). Variations in grain sizes are observed within individual catchments within the Ventura basin but not significant changes in lithology, such as changes from sedimentary rocks to igneous or metamorphic rocks (Fig. 2). Accordingly, we assume that quartz is sourced evenly from throughout the catchments in the study area and that the sediment is well-mixed and homogenized during transport.

An additional assumption when deriving catchment-averaged erosion rates is that catchments are in isotopic equilibrium where the incoming and outgoing isotope (or sediment) fluxes are equal (Bierman and Steig, 1996). Perturbations in the ratio of incoming and outgoing

isotope flux can arise in areas with high-density, deep-seated landslides that mobilize nuclide-depleted sediments from beneath the nuclide production zone (Niemi et al., 2005; Roda-Boluda et al., 2019; Yanites et al., 2009). The influence of landslides on the catchment-averaged erosion rates is discussed in detail in the main manuscript.

We collected 18 samples of ~2 kg of sand-sized sediment using a trowel and we recorded the latitude, longitude, and elevation at the sample location using a handheld GPS. Where possible, we sampled from sand bars indicating recent fluvial transport and located as near as possible to the center of the channel to avoid contamination of the sample from bank collapse or landslides.

2. LABORATORY ANALYSIS AND ACCELERATOR MASS SPECTROMETRY DETAILS

2.1 Laboratory analysis

Beryllium and aluminum isolation followed the methodology of Corbett et al. (2016). Firstly, an in house ^{9}Be carrier spike produced from beryl was added to the samples. For burial dating samples, a commercial SPEX aluminum ICP standard solution was also added to the samples as carrier. For samples processed at the University of Vermont (UVM), ten samples were processed alongside a blank to account for laboratory background contamination and a sample of the CRONUS-N sand (Jull et al., 2015) to assess inter-laboratory reproducibility in results (Tables S9 and S10). Our analyses of CRONUS-N have an average concentration of 2.31×10^{5} +/- 1.78×10^{4} (N = 7; 1σ) ^{10}Be atoms g^{-1} and 1.03×10^{6} +/- 6.53×10^{4} (N = 6; 1σ) ^{26}Al atoms g^{-1}, which are consistent with the standard values of 2.17×10^{5} +/- 0.88×10^{4} ^{10}Be atoms g^{-1} and 1.05×10^{6} +/- 1.06×10^{5} ^{26}Al atoms g^{-1} (Tables 4a and 4b, respectively, of Jull et al., 2015). Samples processed in the CosmIC laboratory at Imperial College London (ICL) were processed in batches of nine alongside one process blank. Prior to dissolution and elemental separation, quartz aliquots were tested for purity using an inductively coupled plasma-optical emission spectrometer (ICP-OES). Pure quartz was dissolved in concentrated HF and HNO_3 before being converted into chloride form by fuming in $HClO_4$, and then diluted in HCl. Be and, if appropriate, Al were isolated in the samples using ion exchange chromatography. Anion exchange with HCl was first employed to remove Fe from the samples. Then cation exchange, firstly with H_2SO_4 and secondly with HCl, was used to isolate Be and Al. Be and Al in solution was precipitated as a beryllium or aluminum hydroxide gel which was either burnt using a Bunsen burner or heated in a muffle furnace to produce beryllium or aluminum oxide. Be as beryllium oxide was mixed with Nb powder, and Al as aluminum oxide was mixed with Ag powder. The mixtures were then transferred into copper cathodes ready for analysis using accelerator mass spectrometry.

2.2 Accelerator mass spectrometry details

Accelerator mass spectrometry (AMS) analysis for sample suites HCR, SLC, OCS, SI5 and BCB took place at the Centre for Accelerator Science at the Australian Nuclear Science and Technology Organization (ANSTO) (Wilcken et al., 2017, 2019). Be standard 01–5–2 with an assumed ^{10}Be/^{9}Be ratio of 8.558×10^{-12} (Nishiizumi et al., 2007) was used to calibrate ^{10}Be/^{9}Be ratios measured in the samples. Measured ^{26}Al/^{27}Al ratios for the burial dating samples (HCR,

SLC, OCS, SI5) were calibrated against Al standard KN 01–4–2 with a nominal $^{26}Al/^{27}Al$ ratio of 3.096×10^{-11} (Nishiizumi, 2004). For sample suites HCR, SLC, OCS, and BCB, during $^{10}Be/^{9}Be$ AMS measurements, BeO^- ion beam currents were 1.2–8.0 μA for the samples and 2.9–9.7 μA for the standards. The average BeO^- ion beam current for the samples was 59% of the average beam current for the primary standard. The range of 1σ analytical uncertainties for $^{10}Be/^{9}Be$ AMS measurements for the samples was 3–12% and boron corrections were <1%. During $^{26}Al/^{27}Al$ AMS measurements for samples HCR, SLC, OCS, Al^- ion beam currents were 0.2–0.6 μA for the samples and 0.3–0.7 μA for the standards. The average Al^- ion beam current for the samples was 77% of the average beam current for the primary standard. The 1σ analytical uncertainties for the $^{26}Al/^{27}Al$ AMS measurements ranged from 4–29%.

Sample suites SLC and OCS were blank corrected for Be using the average of three associated process blanks with measured $^{10}Be/^{9}Be$ AMS ratios of 5.56×10^{-16}, 6.93×10^{-16}, and 5.87×10^{-16} and an average ratio of 6.12×10^{-16} +/– 7.22×10^{-17} (N = 3, 1σ). Total ^{10}Be atoms in each of the three blanks processed alongside these samples was 9190 +/– 2200 atoms, 11180 +/– 2400 atoms, and 9150 +/– 2600 atoms, and the average values used for the blank corrections was 9970 +/– 1180 atoms (derived from the average and standard deviation of the measured AMS ratios; N = 3, 1σ). The overall range in final 1σ analytical uncertainties for measurement of ^{10}Be concentrations was 3–9%. Sample suites SLC and OCS were blank corrected for Al using the average of four associated process blanks with measured $^{26}Al/^{27}Al$ AMS ratios of 1.31×10^{-15}, 9.74×10^{-16}, 9.27×10^{-16}, and 1.13×10^{-15} and an average ratio of 1.13×10^{-15} +/– 2.09×10^{-16} (N = 4, 1σ). Total ^{26}Al atoms in each of the four blanks processed alongside these samples were 76200 +/– 34100 atoms, 52948 +/– 37440 atoms, 50430 +/– 50440 atoms, and 72070 +/– 41620 atoms, and the average value used for the blank correction was 62720 +/– 11600 atoms (N = 4, 1σ). The overall range in final 1σ analytical uncertainties for measurement of ^{26}Al was 5–16%.

Sample suite HCR was blank corrected for Be using the blank processed alongside the samples in the laboratory with a measured $^{10}Be/^{9}Be$ AMS ratio of 5.87×10^{-16}. The total ^{10}Be atoms used for blank correction was 9150 +/– 2600 atoms. The overall range in final 1σ analytical uncertainties for measurement of ^{10}Be concentrations for sample HCR was 3–17%. Sample suite HCR was blank corrected for Al using the blank processed alongside the samples in the laboratory with a measured $^{26}Al/^{27}Al$ AMS ratio of 1.31×10^{-15} and the total ^{26}Al atoms in the blank was 72070 +/– 41620 atoms. The overall range in final 1σ analytical uncertainties for measurement of ^{26}Al for HCR was 4–44%.

Sample suite BCB (the boulder exposure age samples), was processed in two batches and blank corrected using the concentration of the specific blank processed alongside each batch. Measured $^{10}Be/^{9}Be$ AMS ratios for the two process blanks were 7.50×10^{-16} and 6.62×10^{-16} and total ^{10}Be atoms in the two blanks processed were 12110 +/– 4030 atoms and 10700 +/– 3100 atoms. The overall range in final 1σ analytical uncertainties for ^{10}Be measurements in sample suite BCB was 3–4%.

During $^{10}Be/^{9}Be$ AMS measurements for sample suite SI5 at ANSTO, BeO^- ion beam currents were 3.8–5.4 μA for the samples. For $^{10}Be/^{9}Be$ AMS measurements of sample suite SI5, the range of 1σ analytical uncertainties was 5–11% and boron corrections were <1%. During $^{26}Al/^{27}Al$ AMS measurements for SI5, Al^- ion beam currents were 0.3–0.5 μA for the samples and 0.4 μA on average for the standards. The range of 1σ analytical $^{26}Al/^{27}Al$ AMS uncertainties for the samples was 16–27%. Sample suite SI5 was blank corrected for Be and Al using the concentration of the batch-specific process blank that was processed in the same batch as the

samples. The measured $^{10}Be/^{9}Be$ AMS ratio for the Be blank was 1.29×10^{-15} and the total ^{10}Be atoms in the blank was 22490 +/– 2720 atoms. The overall range in final 1σ analytical uncertainties for ^{10}Be measurements for SI5 was 6–20%. The measured $^{26}Al/^{27}Al$ AMS ratio for the Al blank was 1.21×10^{-15} and the total ^{26}Al atoms in the blank was 72570 +/– 36290 atoms. The overall range in final 1σ analytical uncertainties for the measurement of ^{26}Al for SI5 was 21–65%.

AMS analysis for Be and Al for sample suites SGR, SGC2, STL and Al for sample suites SVF and SCG took place at the Scottish Universities Environmental Research Centre (SUERC). Measured $^{10}Be/^{9}Be$ ratios were calibrated using Be standard NIST with an assumed Be ratio of 2.79×10^{-11} (Nishiizumi et al., 2007) and ^{26}Al analyses were normalized to the Z92-0222 standard with nominal $^{26}Al/^{27}Al$ ratio of 4.11×10^{-11}, which is consistent with the values reported in Nishiizumi (2004). For sample suites SGC2, STL, and SGR the average BeO^- ion beam current for the samples was 54% of the average beam current for the primary standard and 1σ analytical uncertainties for the $^{10}Be/^{9}Be$ AMS measurements for the samples ranged from 3–10%. During $^{26}Al/^{27}Al$ AMS measurements the average Al^- ion beam current for the samples was 69% of the average beam current for the primary standard. The range of 1σ analytical uncertainties associated with $^{26}Al/^{27}Al$ AMS measurements was 3–16%. Sample suites STL and SGR were blank corrected for Be using the average of two associated blanks processed alongside the samples with measured $^{10}Be/^{9}Be$ AMS ratios of 2.73×10^{-15} and 3.12×10^{-15} and an average ratio of 2.93×10^{-15} +/– 2.78×10^{-16} (N = 2, 1σ). Total ^{10}Be atoms in each of the two blanks processed alongside these samples was 46366 +/– 7425 atoms and 40645 +/– 6075 atoms, and the average value used for the blank correction was 43510 +/– 4156 atoms (N = 2; 1σ). The final range in overall 1σ analytical uncertainties for measurement of ^{10}Be concentrations was 3–17%.

Sample suites STL and SGR were blank corrected for Al using the average of two associated process blanks with measured $^{26}Al/^{27}Al$ AMS ratios of 6.30×10^{-16} and 3.07×10^{-16} and an average ratio of 4.69×10^{-16} +/– 2.29×10^{-16} (N = 2, 1σ). Total ^{26}Al atoms in each of the two blanks processed alongside these samples was 27755 +/– 19627 atoms and 13254 +/– 13253 atoms and the average value used for the blank correction was 20260 +/– 9900 atoms. The overall range in final 1σ analytical uncertainties for measurement of ^{26}Al for sample suites STL and SGR was 3–15%. Sample suite SGC2 was blank corrected using the blank processed alongside the samples in the laboratory with a measured $^{10}Be/^{9}Be$ AMS ratios of 3.12×10^{-15} and total ^{10}Be of 46366 +/– 7425 atoms. The final range in overall 1σ analytical uncertainties for measurement of ^{10}Be concentrations was 3–32%. Sample suite SGC2 was blank corrected for Al using a process blank with a measured $^{26}Al/^{27}Al$ AMS ratio of 6.30×10^{-16} and total ^{26}Al of 27755 +/– 19627 atoms. The overall range in final 1σ analytical uncertainties for measurement of ^{26}Al for sample suites SGC2 was 6–19%.

AMS ratios for $^{10}Be/^{9}Be$ for sample suites SVF and SCQ and for the erosion rate samples were measured in two separate AMS runs at Lawrence Livermore National Laboratory AMS facility (Rood et al., 2010) and were normalized using Be standard 01–5–4 with an assumed $^{10}Be/^{9}Be$ ratio of 2.851×10^{-12} (Nishiizumi et al., 2007). For sample suites SVF and SCQ, the average BeO^- ion beam current for the samples was 68% of the average beam current for the primary standard. The range of 1σ analytical uncertainties for $^{10}Be/^{9}Be$ AMS measurements for the samples was 3–16%. During $^{26}Al/^{27}Al$ AMS measurements the average Al^- ion beam current for the samples was 79% of the average beam current for the primary standard. The range of 1σ analytical uncertainties associated with the $^{26}Al/^{27}Al$ AMS measurements for the samples was 6–

17%. Sample suites SVF and SCQ were blank corrected for Be using the batch-specific process blank measured with the samples. For SVF and SCQ the measured $^{10}Be/^{9}Be$ AMS ratio for the process blank was 1.97×10^{-15} and the total ^{10}Be in the process blank was 27114 +/– 3906 atoms. The final range in overall 1σ analytical uncertainties for measurement of ^{10}Be concentrations was 2–25%. Sample suites SVF and SCQ were blank corrected for Al using the batch-specific process blank measured with the samples. For SVF and SCQ the measured $^{26}Al/^{27}Al$ AMS ratio for the process blank was 8.35×10^{-16} and the total ^{26}Al was 36414 +/– 21018 atoms. The overall range in total 1σ analytical uncertainties for measurement of ^{26}Al concentrations for these four samples was 7–20%.

During $^{10}Be/^{9}Be$ AMS measurements for the erosion rate samples, $^{9}Be^{3+}$ ion beam currents were 12–22 μA for the samples. The 1σ analytical uncertainties associated with $^{10}Be/^{9}Be$ AMS measurements for the samples ranged from 2–22%. The erosion rate samples were blank corrected using the average of the two blanks processed alongside the samples in the laboratory. The two process blanks had measured $^{10}Be/^{9}Be$ AMS ratios of 1.82×10^{-15} and 1.83×10^{-15} and the average value used for the correction was 1.82×10^{-15} +/– 8.67×10^{-18} (N = 2; 1σ). Total ^{10}Be in each of these blanks was 30933 +/– 4391 atoms and 31126 +/– 4227 atoms, respectively, with an average value of 31029 +/– 136 atoms. The overall range in total 1σ analytical uncertainties for measurement of ^{10}Be concentrations was 2–19%.

3. STREAM POWER, K_{SN}, AND FLUVIAL RESPONSE

On timescales of 10^6–10^7 years, landscapes might be expected to reach a dynamic equilibrium where erosion and rock uplift rates become coupled, like the relationship documented in parts of the Himalaya (Lavé and Avouac, 2001; Finnegan et al., 2008) and the Basin and Range (Densmore et al., 2004). In both transient and steady-state landscapes, longitudinal stream profiles can be defined by a power law function that relates channel gradient, *S*, at a particular down-system point, to upstream drainage area, *A*. For a simple stream power model in a steady-state landscape this can be expressed as

$$S = \left(\frac{U}{K}\right)^{\frac{1}{n}} A^{\frac{-m}{n}} \quad \text{(Equation S1)}$$

where *U* is an uplift rate, *K* is a coefficient that represents bedrock erodibility (amongst other factors) and *m* and *n* are exponents related to erosional dynamics and hydraulic geometry (e.g., Whipple and Tucker, 1999; Tucker and Whipple, 2002). The term $\left(\frac{U}{K}\right)^{\frac{1}{n}}$ can be described as the channel steepness index, k_s, and the ratio of *m/n* as the channel concavity, θ. For a classic unit stream power model, $m = 0.5$, $n = 1$, and $\theta = 0.5$. A reference value of θ is typically used to estimate a normalized channel steepness index, k_{sn}, allowing comparisons in steepness between neighboring river channels with different concavities (e.g., Snyder et al., 2000; Wobus et al., 2006a). The steepness index fundamentally reflects how steep a river is for a given drainage area and has been shown in numerous studies to be sensitive to both uplift and bedrock erodibility (Kirby and Whipple, 2001; Kirby et al., 2003; Cyr et al., 2010; DiBiase et al., 2010; DiBiase and Whipple, 2011; D'Arcy and Whittaker, 2014).

To calculate a reference concavity, we used standard algorithms contained in TopoToolbox (Schwanghart and Scherler, 2014). We initially extracted a stream network with a high drainage density using a low-threshold stream area of 50,000 m^2. We then identified the transition from colluvial to fluvial domains based on the change in gradient on a plot of log-

drainage area versus log-gradient to be around 10^6 m^2 (Figure S2). The slope of a linear regression through the data from drainage areas >10^6 m^2 has a slope of 0.45. However, using a minimum threshold area of 10^6 m^2 results in many streams which underestimate the true stream length as visible in the USGS 10-m digital elevation models (DEM). A minimum threshold area of 0.5×10^6 m^2 returns stream lengths that show a better agreement with what we interpret to be the channel heads in the DEM. With a minimum threshold area of 0.5×10^6 m^2 for the stream's shown in Figure 8A, the slope of the regression of log-drainage area versus log-gradient is 0.48 +/– 0.0004 (errors are one standard error; Figure S2). We use this slope to justify a reference concavity of 0.50.

In order to calculate fluvial response times presented in section 5.3 of the main manuscript we first need to estimate the 'erodibility' parameter *K*. In a simplified stream power erosion law assuming topographic steady state (e.g., Howard and Kerby, 1983; Whipple and Tucker, 2002):

$$U = KA^mS^n, \qquad \text{(Equation S2)}$$

we can rearrange for *K*:

$$K = \frac{U}{A^mS^n} \qquad \text{(Equation S3)}$$

Values for the rock uplift rate (*U*) are based on the values contained in Table 1 and upstream drainage area (*A*) is based on the values in Table 2. We measured slope (*S*) as the average gradient of the entire stream assuming that any knickpoint has propagated up the entire stream length and that any current knickpoints are non-tectonic. In our simplified calculations of *K*, we assume the classic case where the slope exponent (n) is equal to 1 (Howard and Kerby, 1983; Whipple and Tucker, 1999) and extract the drainage area exponent, m, from the reference concavity (θ) of 0.5 with the formula:

$$\theta = \frac{m}{n} \qquad \text{(Equation S4)}$$

Uplift rates are spatially variable, so we calculated local *K* values based on the local uplift rate. We calculated local *K* values in the hanging wall of the Ventura fault based on the uplift rates of the Ventura Avenue anticline (Rockwell et al., 1988; Hubbard et al., 2014) and in the hanging wall of the southern San Cayetano fault based on the uplift rate from Hughes et al. (2018). Local *K* values for the eastern and western sections of the San Cayetano fault were based on the uplift rates re-evaluated here and included in Table 1.

We then input *K* values into the formula for knickpoint celerity (v; Equation 2) to calculate declining v upstream as a function of *A* for each increment (i.e., one cell in the DEM) along the stream:

$$v = KA^mS^{n-1} \text{ (Equation 2),}$$

We convert v to time by dividing the distance between each increment by v and then take the sum of time increments for the length of the stream up to 0.5 km from the drainage divide to represent the fluvial retreat rate.

4. DISCUSSION OF ALTERNATIVE ISOCHRON AGES

We removed sample HCR-2 from the isochron at the base of the Las Posas Formation in the hanging wall of the Ventura fault (isochron HCR) because the sample plotted above the surface production ratio. Including this sample in the regression makes almost no difference to the final isochron age. The slope of isochron HCR is also strongly dependent on the ^{26}Al/^{10}Be ratio of the highest concentration sample, sample HCR-6 (Fig. 4A). If HCR-6 is not included in

the regression, then the isochron produces a burial age of 0.55 $^{+0.15}/_{-0.16}$ Ma, which overlaps in uncertainty with the age of 0.60 $^{+0.05}/_{-0.06}$ Ma that results from including sample HCR-6 (Table S6). Therefore, we can be reasonably confident that the sample HCR-6 is not an outlier.

For our preferred age for the sample suite from the top of the exposed Saugus Formation in the hanging wall of the Ventura fault (isochron SVF), we removed sample SVF-C which has a ^{10}Be concentration >3σ away from the most likely isochron line. We interpret SVF-C as an outlier because the sample plots above the surface production ratio of 6.75 (Fig. 4B). We also removed sample SVF-B, which has an anomalously low ^{26}Al/^{10}Be ratio and has a ^{10}Be concentration more than 3σ away from the most likely isochron line (Fig. 4B). Including both of the aforementioned outliers in the regression makes little difference to the overall age of the isochron. However, removing just sample SVF-C would increase the isochron age to 0.38 $^{+0.56}/_{-0.58}$ Ma, and removing just sample SVF-B would increase the final burial age to 0.50 +/- 0.46 Ma (Table S6). Both alternative ages are within the large uncertainty associated with our preferred age of 0.36 $^{+0.22}/_{-0.18}$ Ma, but we suggest removing both samples from the regression is justified because both meet the criteria to be treated as outliers.

For the Saugus Formation samples from the hanging wall of the Oak Ridge fault, including the sand samples in the regression would lead to burial ages of 1.61 $^{+0.96}/_{-0.98}$ Ma for the isochron from the Happy Camp syncline (isochron SCQ) and 1.15 $^{+0.22}/_{-0.26}$ Ma for the isochron from the Long Canyon syncline (isochron SLC; Table S6). Compared to our preferred younger ages of 1.06 $^{+0.23}/_{-0.26}$ Ma and 0.98 $^{+0.20}/_{-0.28}$ Ma, respectively, the older ages are not consistent with the independent age for the Saugus Formation at Moorpark of 0.78–0.85 Ma (Wagner et al., 2007) and are less consistent with the 1.2 +/– 0.3 Ma age for the Bailey ash mapped several hundred meters stratigraphically below the Saugus Formation in the Pico Formation (Figure 6A; Izett et al., 1974; Boellstorff and Steineck, 1975). The better match of the younger ages with the existing chronology provides further justification for excluding the sand samples for these isochrons. For the isochron from the Grimes Canyon Deltaic facies (isochron SGC2), we removed one sample (SGC2-C) from the regression that has both ^{10}Be and ^{26}Al concentrations much more than 3σ away from the preferred regression line and is clearly an outlier (Fig. 4E).

In the eastern Ventura basin, an alternative burial age for the Sunshine Ranch Member (isochron SI5) is ~5.97 $^{+3.44}/_{-3.50}$ Ma compared with 3.30 $^{+0.30}/_{-0.41}$ Ma if the sand sample (SI5-S) is omitted (Table S6). A slightly older age is still consistent with the age range of 5.3–3.6 suggested by ^{87}Sr/^{86}Sr dating on the underlying Pico Formation (Buczek et al., 2021). However, the younger burial age also overlaps with the ^{87}Sr/^{86}Sr age within the 95% confidence limits and the ^{87}Sr/^{86}Sr age is thought to be an overestimate (Buczek et al., 2021). For our preferred age for the isochron from the upper part of the Saugus Formation (isochron STL) of 0.83 $^{+0.36}/_{-0.41}$ Ma, we omitted the sand sample (STL-7) and the sample STL-3, which has ^{10}Be concentration >3σ away from any possible regression line (Fig. 4G). However, the sand sample could form part of a possible regression line with the four lower concentration samples (Fig. 4G). If we assumed the sand sample was not an outlier, then we would have to treat sample STL-5 as an outlier because in this alternative interpretation the ^{10}Be concentration for sample STL-5 would be much greater than 3σ away from the alternative regression line (Fig. 4G). The alternative interpretation without STL-5 results in a burial age of 2.66 $^{+0.24}/_{-0.30}$ Ma (Table S6). Another alternative isochron including both STL-5 and the sand sample gives a burial age of 2.2 $^{+1.46}/_{-1.48}$ Ma (Table S6). However, both these alternative ages are incompatible with the identification of the 0.76 Ma Bishop ash stratigraphically just below the sample location (Fig. S4; Levi and Yeats, 1993), which further supports our preferred age.

REFERENCES CITED

Balco, G., and Rovey, C.W., 2008, An isochron method for cosmogenic-nuclide dating of buried soils and sediments: American Journal of Science, v. 308, no. 10, p. 1083–1114, https://doi.org/10.2475/10.2008.02.

Balco, G., Stone, J.O., Lifton, N.A., and Dunai, T.J., 2008, A complete and easily accessible means of calculating surface exposure ages or erosion rates from 10 Be and 26 Al measurements: Quaternary Geochronology, v. 3, no. 3, p. 174–195, https://doi.org/10.1016/j.quageo.2007.12.001.

Balco, G., Soreghan, G.S., Sweet, D.E., Marra, K.R., and Bierman, P.R., 2013, Cosmogenic-nuclide burial ages for Pleistocene sedimentary fill in Unaweep Canyon, Colorado, USA: Quaternary Geochronology, v. 18, p. 149–157, https://doi.org/10.1016/j.quageo.2013.02.002.

Behr, W., Rood, D., Fletcher, K., Guzman, N., Finkel, R., Hanks, T.C., Hudnut, K., Kendrick, K., Platt, J., and Sharp, W., 2010, Uncertainties in slip-rate estimates for the Mission Creek strand of the southern San Andreas fault at Biskra Palms Oasis, southern California: Geological Society of America Bulletin, v. 122, no. 9–10, p. 1360–1377, https://doi.org/10.1130/B30020.1.

Bender, A.M., Amos, C.B., Bierman, P., Rood, D.H., Staisch, L., Kelsey, H., and Sherrod, B., 2016, Differential uplift and incision of the Yakima River terraces, central Washington State: Journal of Geophysical Research. Solid Earth, v. 121, no. 1, p. 365–384, https://doi.org/10.1002/2015JB012303.

Bierman, P., and Gillespie, A., 1991, Range fires: A significant factor in exposure-age determination and geomorphic surface evolution: Geology, v. 19, no. 6, p. 641–644, https://doi.org/10.1130/0091-7613(1991)019<0641:RFASFI>2.3.CO;2.

Bierman, P., and Steig, E.J., 1996, Estimating rates of denudation using cosmogenic isotope abundances in sediment: Earth Surface Processes and Landforms, v. 21, no. 2, p. 125–139, https://doi.org/10.1002/(SICI)1096-9837(199602)21:2<125::AID-ESP511>3.0.CO;2-8.

Boellstorff, J.D., and Steineck, P.L., 1975, The stratigraphic significance of fission-track ages on volcanic ashes in the marine late Cenozoic of southern California: Earth and Planetary Science Letters, v. 27, no. 2, p. 143–154, https://doi.org/10.1016/0012-821X(75)90023-0.

Buczek, A.J., Hendy, A.J., Hopkins, M.J. and Sessa, J.A., 2021. On the reconciliation of biostratigraphy and strontium isotope stratigraphy of three southern Californian Plio-Pleistocene formations. Geological Society of America Bulletin, 133(1-2), pp.100-114.

Campbell, R.H., Wills, C.J., Irvine, P.J. and Swanson, B.J., 2014, Preliminary geologic map of the Los Angeles 30′×60′ quadrangle, Southern California: California Geological Survey, scale 1:100,000, p. 2331–1258.

Chmeleff, J., von Blanckenburg, F., Kossert, K., and Jakob, D., 2010, Determination of the 10Be half- life by multicollector ICP-MS and liquid scintillation counting: Nuclear Instruments & Methods in Physics Research. Section B, Beam Interactions with Materials and Atoms, v. 268, no. 2, p. 192–199, https://doi.org/10.1016/j.nimb.2009.09.012.

Çiner, A., Doğan, U., Yıldırım, C., Akçar, N., Ivy-Ochs, S., Alfimov, V., Kubik, P.W., and Schlüchter, C., 2015, Quaternary uplift rates of the Central Anatolian Plateau, Turkey: insights from cosmogenic isochron-burial nuclide dating of the Kızılırmak River terraces:

Quaternary Science Reviews, v. 107, p. 81–97, https://doi.org/10.1016/j.quascirev.2014.10.007.
Corbett, L.B., Bierman, P.R., and Rood, D.H., 2016b, An approach for optimizing in situ cosmogenic ^{10}Be sample preparation: Quaternary Geochronology, v. 33, p. 24–34, https://doi.org/10.1016/j.quageo.2016.02.001.
Cyr, A.J., Granger, D.E., Olivetti, V., and Molin, P., 2010, Quantifying rock uplift rates using channel steepness and cosmogenic nuclide–determined erosion rates: Examples from northern and southern Italy: Lithosphere, v. 2, no. 3, p. 188–198, https://doi.org/10.1130/L96.1.
D'Arcy, M., and Whittaker, A.C., 2014, Geomorphic constraints on landscape sensitivity to climate in tectonically active areas: Geomorphology, v. 204, p. 366–381, https://doi.org/10.1016/j.geomorph.2013.08.019.
Densmore, A.L., Dawers, N.H., Gupta, S., Guidon, R., and Goldin, T., 2004, Footwall topographic development during continental extension: Journal of Geophysical Research. Earth Surface, v. 109, F3.
DeVecchio, D.E., Heermance, R.V., Fuchs, M., and Owen, L.A., 2012a, Climate-controlled landscape evolution in the Western Transverse Ranges, California: Insights from Quaternary geochronology of the Saugus Formation and strath terrace flights: Lithosphere, v. 4, no. 2, p. 110–130, https://doi.org/10.1130/L176.1.
DeVecchio, D.E., Keller, E.A., Fuchs, M., and Owen, L.A., 2012b, Late Pleistocene structural evolution of the Camarillo fold belt: Implications for lateral fault growth and seismic hazard in Southern California: Lithosphere, v. 4, no. 2, p. 91–109, https://doi.org/10.1130/L136.1.
DiBiase, R.A., and Whipple, K.X., 2011, The influence of erosion thresholds and runoff variability on the relationships among topography, climate, and erosion rate: Journal of Geophysical Research. Earth Surface, v. 116, F4.
DiBiase, R.A., Whipple, K.X., Heimsath, A.M., and Ouimet, W.B., 2010, Landscape form and millennial erosion rates in the San Gabriel Mountains, CA: Earth and Planetary Science Letters, v. 289, no. 1–2, p. 134–144, https://doi.org/10.1016/j.epsl.2009.10.036.
Dibblee, T.W., Jr., and Ehrenspeck, H.E., 1988, Geologic map of the Ventura and Pitas Point Quadrangles, Ventura County, California: Dibblee Geological Foundation map, Santa Barbara, California, scale, 1:24,000.
Dibblee, T.W., Jr., and Ehrenspeck, H.E., 1992, Geologic map of the Simi Quadrangle, Ventura County, California: Dibblee Geological Foundation map DF-39, Santa Barbara, California, scale, 1:24,000.
Erlanger, E.D., Granger, D.E., and Gibbon, R.J., 2012, Rock uplift rates in South Africa from isochron burial dating of fluvial and marine terraces: Geology, v. 40, no. 11, p. 1019–1022, https://doi.org/10.1130/G33172.1.
Finnegan, N.J., Hallet, B., Montgomery, D.R., Zeitler, P.K., Stone, J.O., Anders, A.M., and Yuping, L., 2008, Coupling of rock uplift and river incision in the Namche Barwa–Gyala Peri massif, Tibet: Geological Society of America Bulletin, v. 120, no. 1–2, p. 142–155, https://doi.org/10.1130/B26224.1.
Frankel, K.L., Brantley, K.S., Dolan, J.F., Finkel, R.C., Klinger, R.E., Knott, J.R., Machette, M.N., Owen, L.A., Phillips, F.M., Slate, J.L., and Wernicke, B.P., 2007, Cosmogenic Be-10 and Cl-36 geochronology of offset alluvial fans along the northern Death Valley fault zone: Implications for transient strain in the eastern California shear zone: Journal of Geophysical Research. Solid Earth, v. 112, B6.

Granger, D.E., Kirchner, J.W., and Finkel, R., 1996, Spatially averaged long-term erosion rates measured from in situ-produced cosmogenic nuclides in alluvial sediment: The Journal of Geology, v. 104, no. 3, p. 249–257, https://doi.org/10.1086/629823.
Granger, D.E., and Muzikar, P.F., 2001, Dating sediment burial with in situ-produced cosmogenic nuclides: theory, techniques, and limitations: Earth and Planetary Science Letters, v. 188, no. 1–2, p. 269–281, https://doi.org/10.1016/S0012-821X(01)00309-0.
Heyman, J., Applegate, P.J., Blomdin, R., Gribenski, N., Harbor, J.M., and Stroeven, A.P., 2016, Boulder height–exposure age relationships from a global glacial ^{10}Be compilation: Quaternary Geochronology, v. 34, p. 1–11, https://doi.org/10.1016/j.quageo.2016.03.002.
Heirshberg, T.L., 1997, Actualistic petrofacies analysis of the Pliocene-Pleistocene Saugus Formation, Ventura Basin, Southern California: implications for provenance, paleotectonics, and paleogeography [Ph.D. dissertation]: University of California, Los Angeles.
Howard, A.D., and Kerby, G., 1983, Channel changes in badlands: Geological Society of America Bulletin, v. 94, no. 6, p. 739–752, https://doi.org/10.1130/0016-7606(1983)94<739:CCIB>2.0.CO;2.
Hubbard, J., Shaw, J.H., Dolan, J., Pratt, T.L., McAuliffe, L., and Rockwell, T.K., 2014, Structure and Seismic Hazard of the Ventura Avenue Anticline and Ventura Fault, California: Prospect for Large, Multisegment Ruptures in the Western Transverse Ranges: Bulletin of the Seismological Society of America, v. 104, no. 3, p. 1070–1087, https://doi.org/10.1785/0120130125.
Hughes, A., Rood, D.H., Whittaker, A.C., Bell, R.E., Rockwell, T.K., Levy, Y., Wilcken, K.M., Corbett, L.B., Bierman, P.R., DeVecchio, D.E., Marshall, S.T., Gurrola, L.D., and Nicholson, C., 2018, Geomorphic evidence for the geometry and slip rate of a young, low-angle thrust fault: Implications for hazard assessment and fault interaction in complex tectonic environments: Earth and Planetary Science Letters, v. 504, p. 198–210, https://doi.org/10.1016/j.epsl.2018.10.003.
Huftile, G.J., and Yeats, R.S., 1996, Deformation rates across the Placerita (Northridge Mw= 6.7 aftershock zone) and Hopper Canyon segments of the western Transverse Ranges deformation belt: Bulletin of the Seismological Society of America, v. 86, 1B, p. S3–S18.
Izett, G., Naeser, C., and Obradovich, J., 1974, Fission-track age of zircons from an ash bed in the Pico Formation (Pliocene and Pleistocene) near Ventura, California, Geol. Soc. Am. Abstr. Programs, pp. 197.
Jull, A.T., Scott, E.M., and Bierman, P., 2015, The CRONUS-Earth inter-comparison for cosmogenic isotope analysis: Quaternary Geochronology, v. 26, p. 3–10, https://doi.org/10.1016/j.quageo.2013.09.003.
Kirby, E., and Whipple, K., 2001, Quantifying differential rock-uplift rates via stream profile analysis: Geology, v. 29, no. 5, p. 415–418, https://doi.org/10.1130/0091-7613(2001)029<0415:QDRURV>2.0.CO;2.
Kirby, E., Whipple, K.X., Tang, W., and Chen, Z., 2003, Distribution of active rock uplift along the eastern margin of the Tibetan Plateau: Inferences from bedrock channel longitudinal profiles: Journal of Geophysical Research. Solid Earth, v. 108, B4, p. 1–24.
Lal, D., 1988, In situ-produced cosmogenic isotopes in terrestrial rocks: Annual Review of Earth and Planetary Sciences, v. 16, no. 1, p. 355–388, https://doi.org/10.1146/annurev.ea.16.050188.002035.

Lal, D., 1991, Cosmic ray labeling of erosion surfaces: in situ nuclide production rates and erosion models: Earth and Planetary Science Letters, v. 104, no. 2–4, p. 424–439, https://doi.org/10.1016/0012-821X(91)90220-C.
Lal, D., and Peters, B., 1967. Cosmic ray produced radioactivity on the earth, Cosmic Rays II: Springer, p. 551–612.
Lavé, J., and Avouac, J., 2001, Fluvial incision and tectonic uplift across the Himalayas of central Nepal: Journal of Geophysical Research. Solid Earth, v. 106, B11, p. 26561–26591, https://doi.org/10.1029/2001JB000359.
Levi, S., and Yeats, R.S., 1993, Paleomagnetic Constraints on the Initiation of Uplift on the Santa-Susana Fault, Western Transverse Ranges, California: Tectonics, v. 12, no. 3, p. 688–702, https://doi.org/10.1029/93TC00133.
Lifton, N., Caffee, M., Finkel, R., Marrero, S., Nishiizumi, K., Phillips, F.M., Goehring, B., Gosse, J., Stone, J., and Schaefer, J., 2015, In situ cosmogenic nuclide production rate calibration for the CRONUS-Earth project from Lake Bonneville, Utah, shoreline features: Quaternary Geochronology, v. 26, p. 56–69, https://doi.org/10.1016/j.quageo.2014.11.002.
Mudd, S.M., Harel, M.-A., Hurst, M.D., Grieve, S.W., and Marrero, S.M., 2016, The CAIRN method: automated, reproducible calculation of catchment-averaged denudation rates from cosmogenic nuclide concentrations: Earth Surface Dynamics, v. 4, no. 3, p. 655–674, https://doi.org/10.5194/esurf-4-655-2016.
Niemi, N.A., Oskin, M., Burbank, D.W., Heimsath, A.M., and Gabet, E.J., 2005, Effects of bedrock landslides on cosmogenically determined erosion rates: Earth and Planetary Science Letters, v. 237, no. 3–4, p. 480–498, https://doi.org/10.1016/j.epsl.2005.07.009.
Nishiizumi, K., 2004, Preparation of ^{26}Al AMS standards: Nuclear Instruments & Methods in Physics Research. Section B, Beam Interactions with Materials and Atoms, v. 223–224, p. 388–392, https://doi.org/10.1016/j.nimb.2004.04.075.
Nishiizumi, K., Winterer, E., Kohl, C., Klein, J., Middleton, R., Lal, D., and Arnold, J., 1989, Cosmic ray production rates of ^{10}Be and ^{26}Al in quartz from glacially polished rocks: Journal of Geophysical Research. Solid Earth, v. 94, B12, p. 17907–17915, https://doi.org/10.1029/JB094iB12p17907.
Nishiizumi, K., Imamura, M., Caffee, M.W., Southon, J.R., Finkel, R.C., and McAninch, J., 2007, Absolute calibration of 10Be AMS standards: Nuclear Instruments & Methods in Physics Research. Section B, Beam Interactions with Materials and Atoms, v. 258, no. 2, p. 403–413, https://doi.org/10.1016/j.nimb.2007.01.297.
Owen, L.A., Clemmens, S.J., Finkel, R.C., and Gray, H., 2014, Late Quaternary alluvial fans at the eastern end of the San Bernardino Mountains, Southern California: Quaternary Science Reviews, v. 87, p. 114–134, https://doi.org/10.1016/j.quascirev.2014.01.003.
Rockwell, T., Keller, E., and Dembroff, G., 1988, Quaternary rate of folding of the Ventura Avenue anticline, western Transverse Ranges, southern California: Geological Society of America Bulletin, v. 100, no. 6, p. 850–858, https://doi.org/10.1130/0016-7606(1988)100<0850:QROFOT>2.3.CO;2.
Roda-Boluda, D.C., D'Arcy, M., Whittaker, A.C., Gheorghiu, D.M., and Rodés, Á., 2019, 10Be erosion rates controlled by transient response to normal faulting through incision and landsliding: Earth and Planetary Science Letters, v. 507, p. 140–153, https://doi.org/10.1016/j.epsl.2018.11.032.
Rood, D.H., Hall, S., Guilderson, T.P., Finkel, R.C., and Brown, T.A., 2010, Challenges and opportunities in high-precision Be-10 measurements at CAMS: Nuclear Instruments &

Methods in Physics Research. Section B, Beam Interactions with Materials and Atoms, v. 268, no. 7–8, p. 730–732, https://doi.org/10.1016/j.nimb.2009.10.016.
Rood, D.H., Burbank, D.W., and Finkel, R.C., 2011, Chronology of glaciations in the Sierra Nevada, California, from ^{10}Be surface exposure dating: Quaternary Science Reviews, v. 30, no. 5–6, p. 646–661, https://doi.org/10.1016/j.quascirev.2010.12.001.
Schwanghart, W., and Scherler, D., 2014, Short Communication: TopoToolbox 2 - MATLAB-based software for topographic analysis and modeling in Earth surface sciences: Earth Surface Dynamics, v. 2, p. 1–7, https://doi.org/10.5194/esurf-2-1-2014.
Snyder, N.P., Whipple, K.X., Tucker, G.E., and Merritts, D.J., 2000, Landscape response to tectonic forcing: Digital elevation model analysis of stream profiles in the Mendocino triple junction region, northern California: Geological Society of America Bulletin, v. 112, no. 8, p. 1250–1263, https://doi.org/10.1130/0016-7606(2000)112<1250:LRTTFD>2.0.CO;2.
Stone, J.O., 2000, Air pressure and cosmogenic isotope production: Journal of Geophysical Research. Solid Earth, v. 105, B10, p. 23753–23759, https://doi.org/10.1029/2000JB900181.
Tucker, G., and Whipple, K., 2002. Topographic outcomes predicted by stream erosion models: Sensitivity analysis and intermodel comparison. Journal of Geophysical Research: Solid Earth, v. 107, no. B9, p. 1–1–1–16.
Wagner, H.M., Lander, B., Roeder, M.A., Prothero, D.R., McDaniel, G.E., Jr., 2007, A new Irvingtonian land mammal assemblage from the Saugus Formation, Moorpark, Ven- tura County, California: Bulletin of the Southern California Academy of Sciences, v. 106, no. 2, p. 141.
Wehmiller, J., Lajoie, K., Sarna-Wojcicki, A., Yerkes, R., Kennedy, G., Stephens, T., Kohl, R., and Zartman, R., 1978, Amino acid racemization dating of Quaternary mollusks, Pacific coast United States: U.S. Geological Survey Open-File Report, v. 78, no. 701, p. 445–448.
Wesnousky, S.G., Briggs, R.W., Caffee, M.W., Ryerson, F., Finkel, R.C., and Owen, L.A., 2016, Terrestrial cosmogenic surface exposure dating of glacial and associated landforms in the Ruby Mountains-East Humboldt Range of central Nevada and along the northeastern flank of the Sierra Nevada: Geomorphology, v. 268, p. 72–81, https://doi.org/10.1016/j.geomorph.2016.04.027.
Whipple, K.X., and Tucker, G.E., 1999, Dynamics of the stream-power river incision model: Implications for height limits of mountain ranges, landscape response timescales, and research needs: Journal of Geophysical Research. Solid Earth, v. 104, B8, p. 17661–17674, https://doi.org/10.1029/1999JB900120.
Whipple, K.X., and Tucker, G.E., 2002, Implications of sediment-flux-dependent river incision models for landscape evolution: Journal of Geophysical Research. Solid Earth, v. 107, B2, p. ETG-3.
Wilcken, K., Fink, D., Hotchkis, M., Garton, D., Button, D., Mann, M., Kitchen, R., Hauser, T., and O'Connor, A., 2017, Accelerator Mass Spectrometry on SIRIUS: New 6MV spectrometer at ANSTO: Nuclear Instruments and Methods in Physics Research Section B, v. 406, p. 278–282, https://doi.org/10.1016/j.nimb.2017.01.003.
Wilcken, K.M., Fujioka, T., Fink, D., Fülöp, R.H., Codilean, A.T., Simon, K., Mifsud, C., and Kotevski, S., 2019, SIRIUS Performance: 10Be, 26Al and 36Cl measurements at ANSTO. Nucl. Instruments Methods Phys. Res. Sect. B Beam Interact. with Mater: Atoms, v. 455, p. 300–304, https://doi.org/10.1016/j.nimb.2019.02.009.
Wobus, C., Whipple, K.X., Kirby, E., Snyder, N., Johnson, J., Spyropolou, K., Crosby, B., Sheehan, D., and Willett, S., 2006a, Tectonics from topography: Procedures, promise, and

pitfalls: Geological Society of America. Special Paper, v. 398, p. 55–74, https://doi.org/10.1130/2006.2398(04).
Yanites, B.J., Tucker, G.E., and Anderson, R.S., 2009, Numerical and analytical models of cosmogenic radionuclide dynamics in landslide-dominated drainage basins: Journal of Geophysical Research. Earth Surface, v. 114, F1.
Yeats, R.S., 1988, Late Quaternary slip rate on the Oak Ridge fault, Transverse Ranges, California: Implications for seismic risk: Journal of Geophysical Research, v. 93, B10, p. 12137–12149, https://doi.org/10.1029/JB093iB10p12137.
York, D., 1966, Least-squares fitting of a straight line: Canadian Journal of Physics, v. 44, no. 5, p. 1079–1086.

A: *Present day*

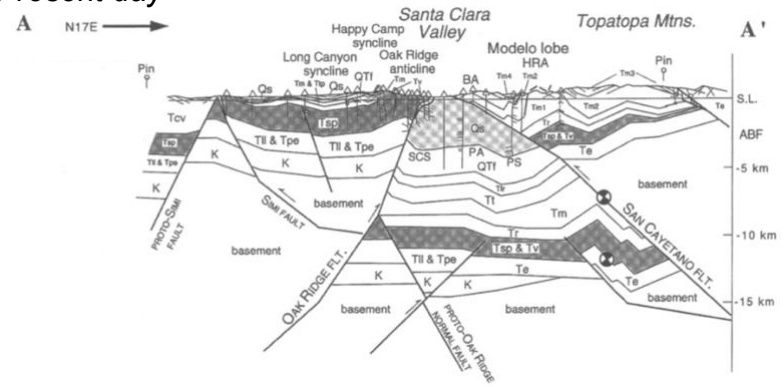

B: *0.7–1.29 Ma (0.5 Ma)*

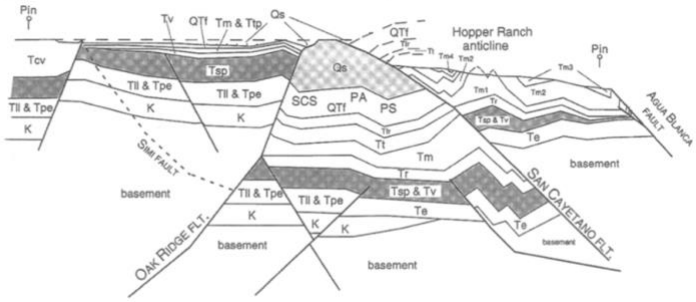

C: *0.94–1.18 Ma (0.975 Ma)*

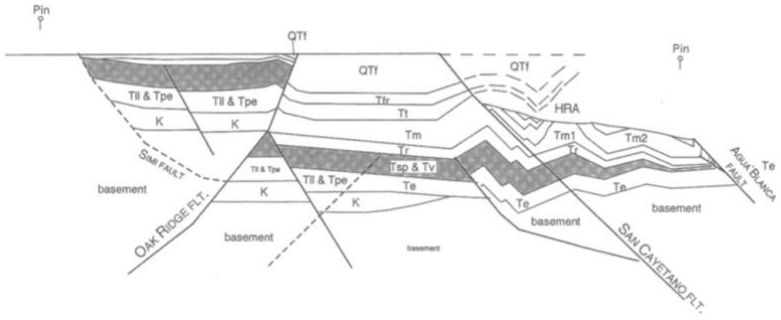

Figure S1. Balanced cross sections through the Long Canyon syncline taken from Huftile and Yeats (1996). The dip-slip offsets, which are included in Table 1, were calculated in Huftile and Yeats (1996) by retro-deforming these balanced cross sections. (A) Present day. (B) Retro-deformed to the top of the exposed Saugus Formation. (C) Retro-deformed to the base of the Las Posas Formation. Ages in boxes refer to the isochron burial ages for the appropriate horizon and the age in brackets below refers to the age interpretation for the same horizon in Huftile and Yeats (1996). Line of section is included on Figure 1.

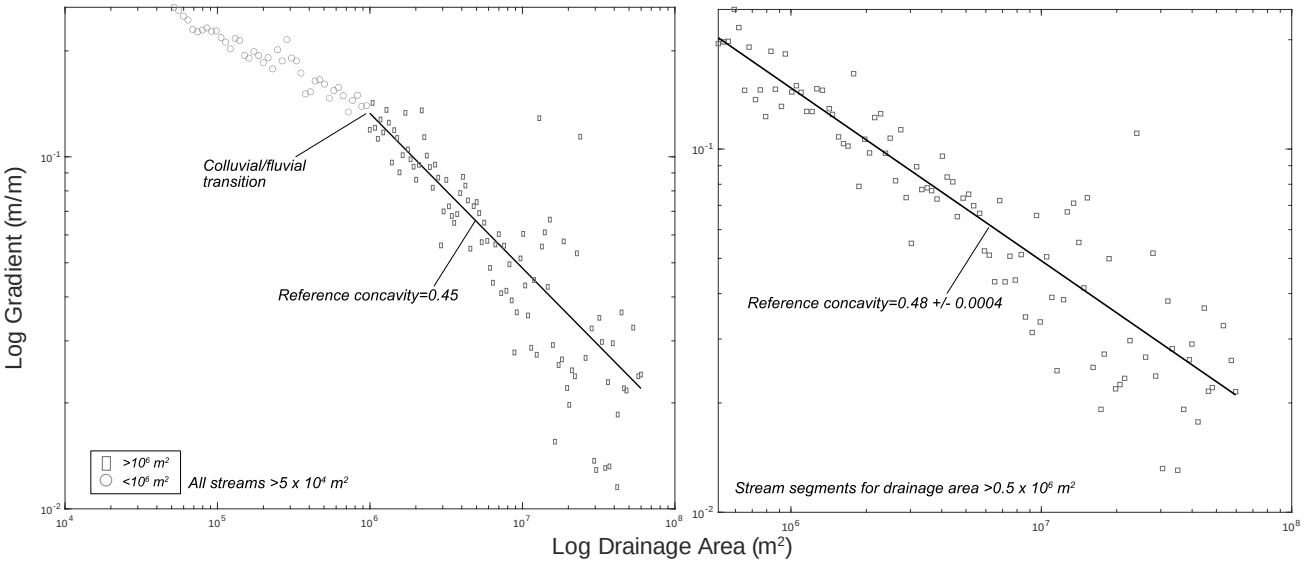

Figure S2. Log-gradient as a function of log-drainage area for the study area. The plot on the left is for all streams with upstream drainage area >50,000 m^2, which indicates a threshold drainage area of 10^6 m^2. However, using a threshold drainage area of 10^6 m^2 results in stream heads that are not consistent with stream heads visible in the 10 m^2 digital elevation model. The plot on the right is for all stream segments shown in figure 8A with drainage area $>0.5 \times 10^6$ m^2. The slope of 0.48 ± 0.0004 (error is one standard error) in the plot on the right is used to justify our reference concavity of 0.50.

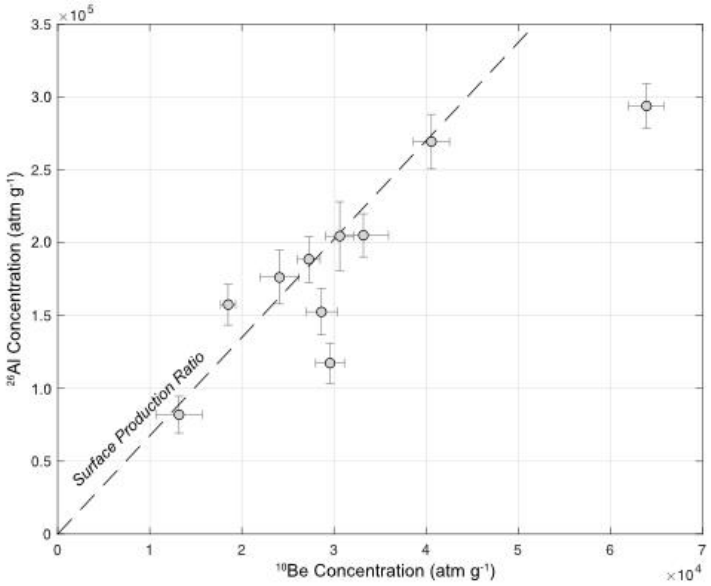

Figure S3. A plot of ^{26}Al-^{10}Be concentrations (gray circles) for the burial dating samples collected from the top of the exposed Saugus Formation in the hanging wall of the Southern San Cayetano fault. Error bars are 1σ. Several of the samples are indistinguishable from the surface production ratio (dashed black line), which indicates that they may be too young for ^{26}Al/^{10}Be isochron burial dating.

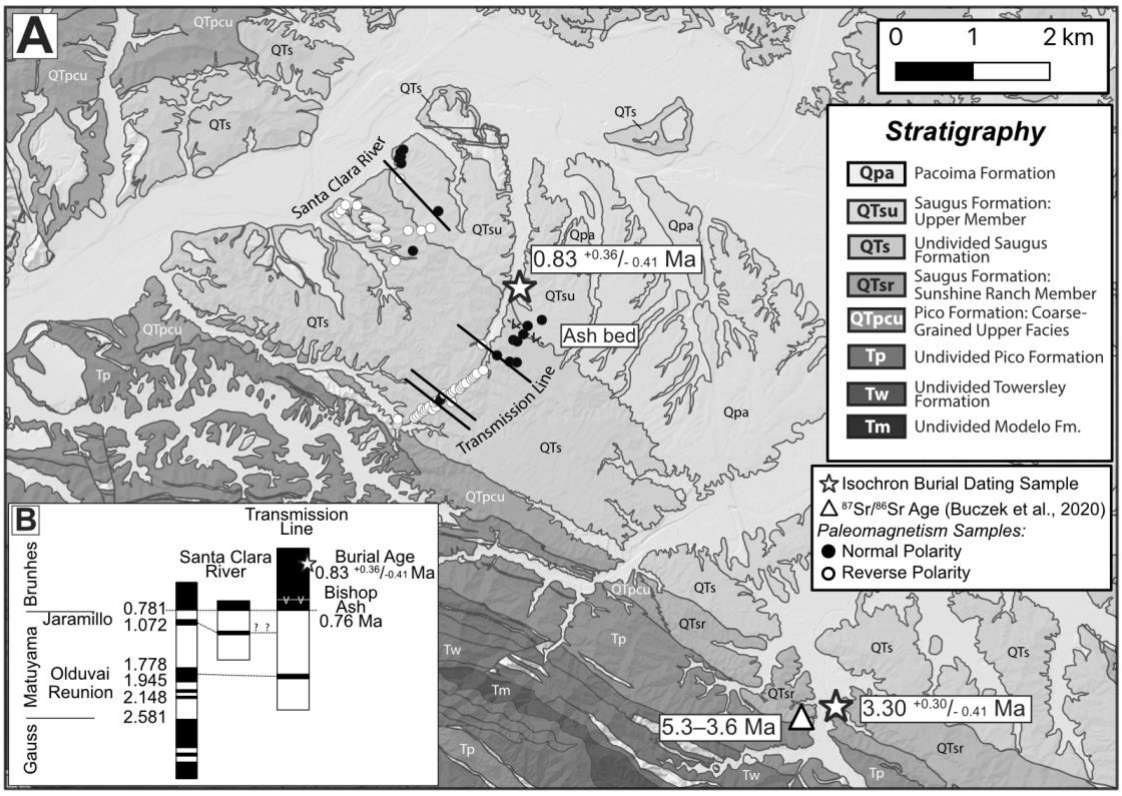

Figure S4. (A) Geological map showing the location of isochron burial dating samples (stars) in the eastern Ventura basin. Mapped geological units are from Campbell et al. (2014). The colored circles represent the locations of paleomagnetic samples, which along with the location of the ash layer (dashed line with v's), are taken from Levi and Yeats (1993). Map location is shown on Figure 1. (B) Interpretation of the paleomagnetic samples from Levi and Yeats (1993) based on the correlation of the ash layer in the Saugus Formation with the 0.76 Ma Bishop Ash.

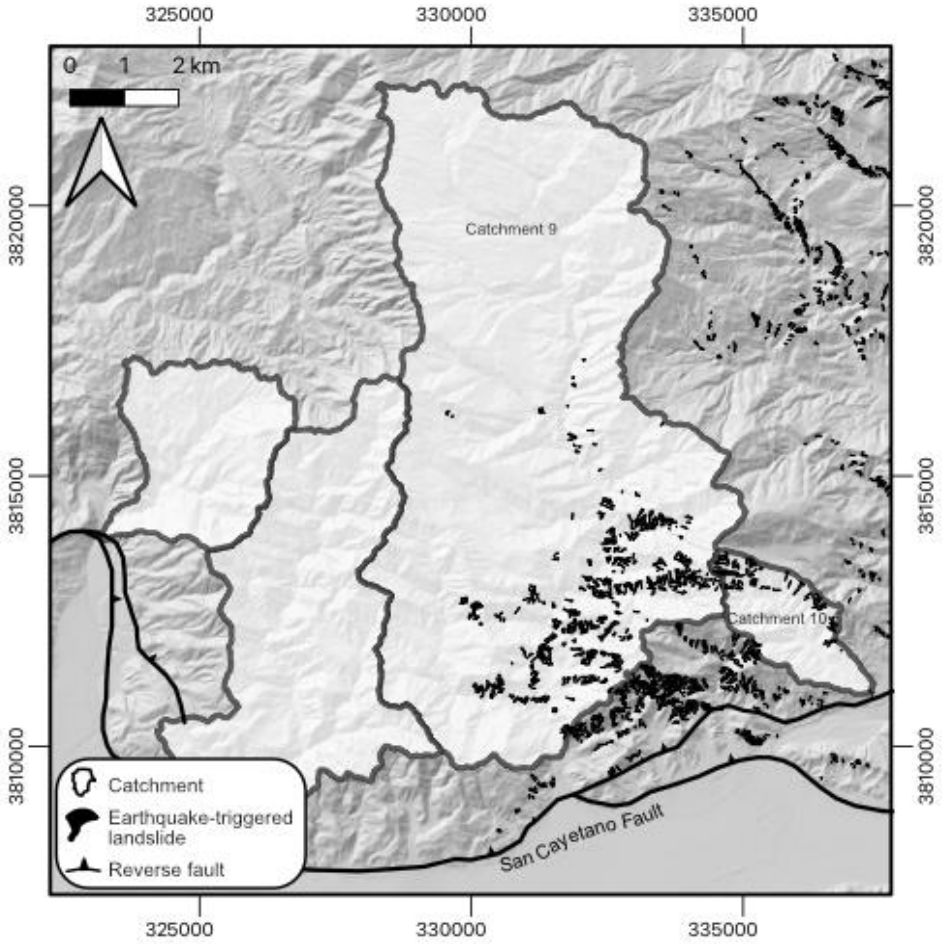

Figure S5. Landslides in the hanging wall of the eastern section of the San Cayetano fault triggered by the 1994 M 6.7 Northridge earthquake. Landslides originally mapped by Harp and Jibson (1995) and recently amended by Townsend et al. (2020). Northridge earthquake landslides cover 2% of the surface area of catchment 9 and 5% of the surface area of catchment 10.

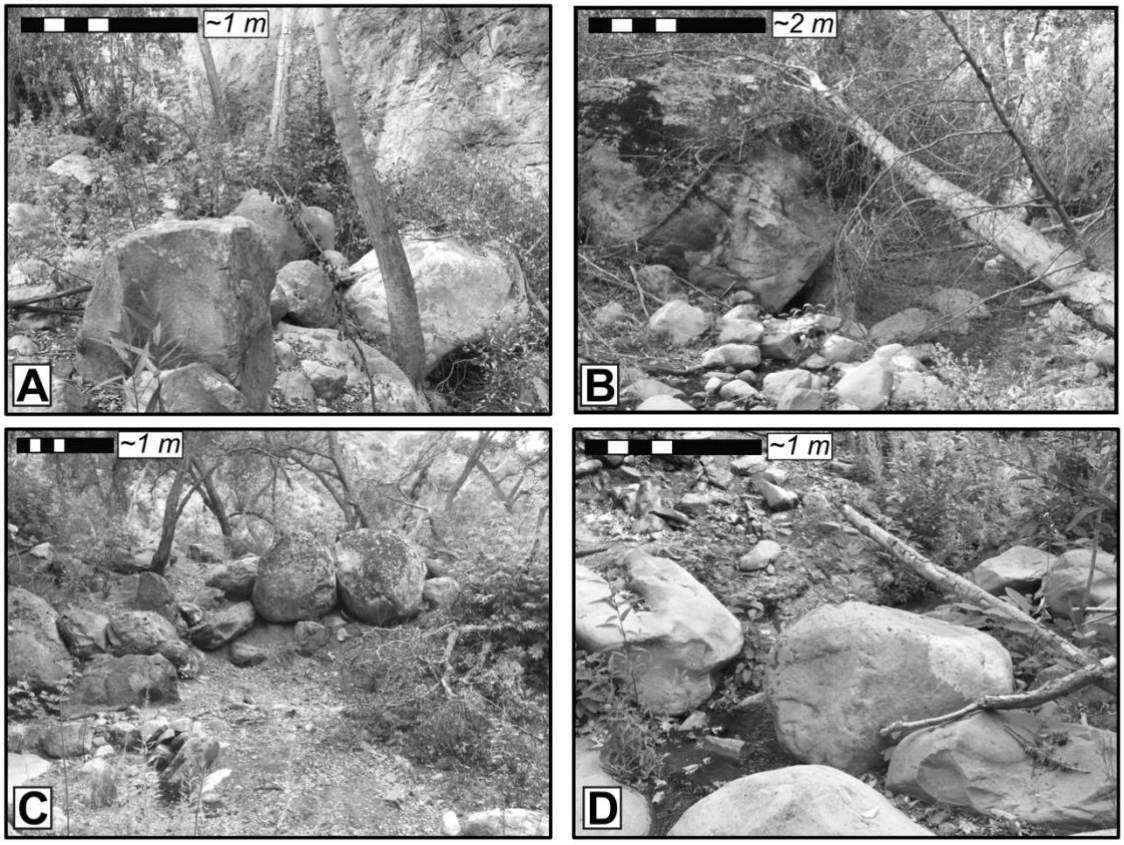

Figure S6. Photos showing large boulders in Sisar Creek (catchment 5). Boulders occasionally in excess of 2 m tall may amour the channel, decrease channel incision, and, therefore, decrease erosion rates measured from channel sands. Photo locations: (A) Lat: 34° 27’ 16.662” N, Lon: 119° 8’ 2.93” W; (B) Lat: 34° 27’ 44.502” N, Lon: 119° 7’ 49.94” W; (C) Lat: 34° 27’ 16.62” N, Lon: 119° 8’ 2.88” W; (D) Lat: 34° 27’ 52.482” N, Lon: 119° 7’ 48.99” W. Photos provided by Brian Swanson.

Table S1. Sensitivity analysis addressing the incorporation of uncertainty in $^{26}Al/^{10}Be$ production ratio into burial ages

Sample	Preferred Age +/- 95% CI R_{sp}= 6.75 (Ma)	Preferred Age Range (Ma)	Age R_{sp}= 6.25 (Ma)	Age R_{sp}= 7.25 (Ma)	Age R_{sp}= 6.69 (Ma)	Age R_{sp}= 7.28 (Ma)
Top Saugus, East Ventura Basin (STL)	$0.83^{+0.36}/_{-0.41}$	0.42–1.19	0.67	0.98	0.81	0.99
Top Saugus, Ventura (SVF)	$0.36^{+0.18}/_{-0.22}$	0.14–0.54	0.20	0.51	0.34	0.52
Base GCDF, Oak Ridge (SGC2)	$1.06^{+}/_{-}$ 0.12	0.93–1.18	*0.90*	*1.20*	1.04	*1.21*
Saugus, Long Canyon Syncline (SLC)	$1.06^{+0.23}/_{-0.26}$	0.80–1.29	0.90	1.21	1.04	1.22
Base Las Posas, Ventura (HCR)	$0.60^{+0.05}/_{-0.06}$	0.54–0.65	*0.39*	*0.70*	0.53	*0.70*
Top Saugus, Happy Camp Syncline (SCQ)	$0.98^{+0.20}/_{-0.28}$	0.70–1.18	0.82	1.13	0.96	1.13
Base Sunshine Ranch, East Ventura Basin (SI5)	$3.30^{+0.30}/_{-0.41}$	2.89–3.60	3.14	3.45	3.28	3.46

R_{sp} is the reference surface production ratio of $^{26}Al/^{10}B$ and is equal to R_{in} from equation 1 of the main manuscript.
R_{sp} values of 6.25 and 7.25 represent the upper and lower bounds of the 1σ uncertainty associated with the standard reference production ratio of 6.75 +/- 0.5 based on Nishiizumi et al. [1989] and normalized to standard values presented in Nishiizumi et al. [2007].
R_{sp} values of 6.69 and 7.28 represent upper and lower bounds of the 95% confidence limits of the slope of our isochron for samples collected in the modern San Gabriel River that were analyzed to validate the use of the standard reference surface production ratio.
Ages in italics indicate that the age based on an alternative R_{sp} lies outside of the 95 % confidence limits of the most likely burial age based on the standard reference production ratio of 6.75.
Uncertainties for ages with alternative R_{sp} are the same as for the preferred age using R_{sp} = 6.75.

Table S2. Full sample parameters for isochron burial dating samples

Stratigraphic Unit	*Sample ID*	*Type*	*Latitude °N (DD.DD, WGS84)*	*Longitude °W (DD.DD, WGS84)*	*Altitude (m.a.s.l)* [a]	*Depth below surface (m)*	*Preferred Isochron Burial Age +/- 95% CI (Ma)* [b]
Top Saugus, Ventura fault	SVF-A	Clast	34.28416	-119.29222	56	2.0 +/- 0.2	0.38 +0.18/-0.22
	SVF-B	Clast					
	SVF-C	Clast					
	SVF-D	Clast					
	SVF-E	Clast					
	SVF-F	Clast					
	SVF-P	Pebbles					
	SVF-S	Sand					
Base Las Posas, Ventura fault	HCR-2	Clast	34.29398	-119.25771	104	3.5 +/- 0.4	0.55 +0.08/-0.07
	HCR-3	Clast					
	HCR-6	Clast					
	HCR-7	Clast					
	HCR-8	Clast					
	HCR-10	Clast					
	HCR-S	Sand					
	HRC-P	Pebbles					
Top Saugus, Happy Camp syncline	SCQ-A	Clast	34.34104	-118.875349	488	2.0 +/- 0.2	0.98 +0.20/-0.28
	SCQ-E	Clast					
	SCQ-F	Clast					
	SCQ-P	Pebbles					
	SCQ-S	Sand					
Top Saugus, Long Canyon syncline	SLC-A	Clast	34.31528	-118.933334	273	3.8 +/- 0.3	1.06 +0.23/-0.26
	SCL-B	Clast					
	SLC-C	Clast					
	SLC-D	Clast					
	SLC-I	Clast					
	SLC-J	Clast					
	SLC-P	Pebbles					
	SLC-S	Sand					
Base GCDF+, Oak Ridge fault	SGC2-E	Clast	34.27778	-118.9075	323	2.0 +/- 0.2	1.06 +/- 0.12
	SGC2-A	Clast					
	SGC2-B	Clast					
	SGC2-C	Clast					
	SGC2-G	Clast					
	SGC2-S	Sand					
Upper Saugus, east Ventura basin	STL-3	Clast	34.41155	-118.59975	450	4.0 +/- 0.2	0.83 +0.36/-0.41
	STL-6	Clast					
	STL-1	Clast					
	STL-2	Clast					

Table S2. Full sample parameters for isochron burial dating samples (continued)

	STL-5	Clast					
	STL-7	Sand					
	STL-8	Pebbles					
Base Sunshine Ranch, east Ventura basin	SI5-F	Clast	34.36167	-118.55417	415	25.0 +/- 1.0	3.30 +0.30/0.41
	SI5-M	Clast					
	SI5-N	Clast					
	SI5-O	Clast					
	SI5-P	Pebbles					
	SI5-S	Sand					
	SI5-U	Clast					
	SI5-V	Clast					
	SI5-X	Clast					
Top Saugus, Southern San Cayetano fault	OCS-1	Clast	34.37591	-119.04053	188	3.0 +/- 0.4	n/a
	OCS-3	Clast					
	OCS-6	Clast					
	OCS-7	Clast					
	OCS-8	Clast					
	OCS-9	Clast					
	OCS-10	Clast					
	OCS-S	Sand					
	OCS-P	Pebbles					

a: Meters above sea level

b: Age and uncertainties calculated using Bayesian linear regression method (Bender et al., 2016)

+ GCDF = Grimes Canyon Deltaic Facies

Table S2. Full sample parameters for isochron burial dating samples (continued)

Sample ID	*Quartz mass (g)*	*Be Cathode ID*	*Be Carrier (g)*[a]	*$^{10}Be/^{9}Be$ AMS*[b,c]	*$^{10}Be/^{9}Be$ AMS 1 σ uncert*[b,c]	*^{10}Be Concentration (atoms g^{-1} SiO_2)*[d]	*^{10}Be 1 σ uncert (atoms g^{-1} SiO_2)*[e]	*^{10}Be 1 σ uncert (%)*	*Al Cathode ID*	*Total Al (µg)*	*$^{26}Al/^{27}Al$ AMS*[c,f]	*$^{26}Al/^{27}Al$ AMS 1 σ*	*^{26}Al Concentration (atoms g^{-1} SiO_2)*[g]	*^{26}Al 1 σ uncert (atoms g^{-1} SiO_2)*[e]	*^{26}Al 1 σ uncert (%)*
SVF-A	20.9960	BE37797	1.0059	1.292E-14	6.578E-16	7145	468	6.5	a2059	2124	2.121E-14	2.28E-15	46002	5269	11.5
SVF-B	11.9290	BE37798	1.0069	8.203E-15	5.107E-16	7163	672	9.4	a2061	2001	8.995E-15	1.55E-15	30554	6061	19.8
SVF-C	17.1940	BE37799	1.0062	6.053E-15	5.144E-16	3252	469	14.4	a2062	2292	1.268E-14	1.89E-15	35241	5814	16.5
SVF-D	25.9510	BE37800	1.0052	9.256E-15	5.563E-16	3843	330	8.6	a2063	2207	1.384E-14	2.00E-15	24677	3907	15.8
SVF-E	32.0420	BE37801	1.0055	1.541E-14	8.724E-16	5747	392	6.8	a2064	2117	2.991E-14	2.56E-15	42863	3844	9.0
SVF-F	21.7560	BE37800	1.0049	1.468E-14	7.478E-16	7998	504	6.3	a2065	2157	2.430E-14	2.25E-15	51918	5090	9.8
SVF-P	9.1140	BE37803	1.0042	6.166E-15	1.007E-15	6292	1571	25.0	a2068	2183	1.002E-14	1.75E-15	49105	9688	19.7
SVF-S	36.5640	BE37804	1.0046	4.273E-14	1.456E-15	15262	556	3.6	a2069	2590	5.728E-14	3.79E-15	89224	6042	6.8
HCR-2	13.7900	BE790	0.8414	4.689E-15	4.90E-16	4808	606	12.6	AL880	2415	1.290E-14	2.317E-15	45312	9529	21.0
HCR-3	11.8968	BE791	0.8396	2.917E-15	3.61E-16	3159	537	17.0	AL881	2451	5.009E-15	1.446E-15	17003	7503	44.1
HCR-6	20.8499	BE792	0.8414	1.100E-13	3.04E-15	84838	2357	2.8	AL882	2518	1.673E-13	6.371E-15	447446	17290	3.9
HCR-7	18.5203	BE793	0.8391	1.922E-14	9.52E-16	16220	841	5.2	AL883	2425	2.726E-14	2.782E-15	75815	8424	11.1
HCR-8	21.3362	BE794	0.8388	1.229E-14	6.92E-16	8840	537	6.1	AL884	2461	1.582E-14	1.919E-15	37361	5310	14.2
HCR-10	17.1301	BE796	0.8409	4.060E-15	3.91E-16	3275	399	12.2	AL886	2371	7.021E-15	1.532E-15	17642	5278	29.9
HCR-S	21.0057	BE798	0.8347	2.476E-14	1.06E-15	18456	822	4.5	AL888	2475	2.702E-14	4.191E-15	95423	10170	10.7
HCR-P	18.4683	BE797	0.8401	1.206E-14	6.99E-16	10027	627	6.3	AL887	1976	4.127E-14	2.352E-15	67601	6497	9.6
SCQ-A	30.7230	BE37805	1.0056	3.078E-14	9.986E-16	12852	463	3.6	a2070	1973	5.255E-14	3.486E-15	74119	5044	6.8
SCQ-E	32.0030	BE37806	1.0052	6.656E-14	2.423E-15	27652	1044	3.8	a2071	2253	9.187E-14	5.923E-15	143058	9338	6.5
SCQ-F	22.9320	BE37807	1.0043	1.804E-14	8.650E-16	9589	544	5.7	a2072	1251	6.006E-14	4.045E-15	72119	4960	6.9
SCQ-P	6.4370	BE37808	1.0064	8.526E-15	7.436E-16	13957	1696	12.2	a2074	1965	1.168E-14	1.673E-15	73898	11862	16.1
SCQ-S	37.8470	BE37809	1.0057	7.063E-14	1.569E-15	24868	577	2.3	a2075	2325	7.582E-14	4.978E-15	102796	6856	6.7
SLC-A	16.3937	BE726	0.8365	2.401E-14	1.131E-15	23546	1141	4.8	AL857	2231	4.249E-14	2.688E-15	125635	8191	6.5
SLC-B	20.2337	BE727	0.8338	3.203E-14	1.158E-15	25534	943	3.7	AL858	2437	5.629E-14	3.822E-15	148287	10290	6.9
SLC-C	21.3569	BE799	0.8345	6.319E-14	1.961E-15	46982	1473	3.1	AL889	2905	7.242E-14	3.867E-15	216399	11756	5.4
SLC-D	19.2653	BE728	0.8477	2.988E-14	1.412E-15	24744	1195	4.8	AL859	2299	5.510E-14	4.227E-15	143756	11273	7.8
SLC-I	14.8049	BE729	0.8430	2.090E-14	8.365E-16	22196	919	4.1	AL860	2413	3.389E-14	2.939E-15	119184	10719	9.0
SLC-J	19.8994	BE732	0.8399	3.299E-14	1.514E-15	26258	1229	4.7	AL863	2505	5.557E-14	3.215E-15	152940	9051	5.9
SLC-P	11.5116	BE731	0.8399	1.179E-14	6.248E-16	15670	882	5.6	AL862	2390	2.733E-14	4.12E-15	121401	19118	15.7
SLC-S	17.5294	BE733	0.8380	3.769E-14	1.268E-15	34057	1167	3.4	AL864	2472	5.068E-14	4.111E-15	155944	12956	8.3
SGC2E	23.8788	b7751	0.6999	8.147E-14	2.472E-15	48821	1572	3.2	a1890	4621	4.921E-14	2.783E-15	209791	12173	5.8
SGC2A	23.0499	b7752	0.6966	2.464E-14	1.152E-15	13822	807	5.8	a1891	2111	1.578E-14	1.555E-15	30965	3306	10.7
SGC2B	23.0759	b7753	0.6981	1.091E-14	7.896E-16	5007	601	12.0	a1892	1974	1.375E-14	1.599E-15	25052	3169	12.7
SGC2C	14.8560	b7755	0.6979	5.385E-15	5.329E-16	2255	729	32.3	a1894	2017	7.257E-15	1.193E-15	20081	3859	19.2

Table S2. Full sample parameters for isochron burial dating samples (continued)

SGC2G	19.2320	b7757	0.6971	1.562E-14	8.928E-16	9615	787	8.2	a1896	2039	1.602E-14	1.728E-15	36412	4222	11.6
SGC2S	22.8815	b7758	0.6958	2.706E-14	1.353E-15	15519	935	6.0	a1897	2259	2.887E-14	2.129E-15	62246	4794	7.7
STL-3	12.7896	b7761	0.6955	9.012E-15	7.003E-16	7034	871	12.4	a1900	1983	1.525E-14	2.225E-15	51141	7739	15.1
STL-6	22.7830	b7765	0.6978	2.240E-14	1.292E-15	12664	859	6.8	a1904	1993	2.697E-14	2.000E-15	51735	3930	7.6
STL-1	13.2606	b7773	0.6979	9.486E-15	9.542E-16	7338	1112	15.2	a1912	1921	1.255E-14	1.831E-15	39058	5966	15.3
STL-2	21.9948	b7774	0.6978	1.317E-14	7.645E-16	6908	549	7.9	a1913	1991	1.965E-14	2.157E-15	38750	4383	11.3
STL-5	6.3629	b7777	0.6974	1.010E-14	6.808E-16	16712	1714	10.3	a1916	2056	1.396E-14	1.833E-15	97261	13319	13.7
STL-7	21.9246	b7778	0.6907	3.432E-14	1.258E-15	21024	863	4.1	a1917	2055	3.120E-14	2.452E-15	64293	5153	8.0
STL-8	15.6834	b7779	0.7020	1.261E-14	6.863E-16	9215	705	7.6	a1918	1938	1.701E-14	2.018E-15	45616	5602	12.3
SI5-F	29.5560	XBE0295	0.335	6.868E-15	5.458E-16	3230	328	10.2	XAL0050	1573	7.643E-15	1.373E-15	7634	1783	23.4
SI5-M	30.1570	XBE0296	0.336	1.584E-14	8.278E-16	8203	475	5.8	XAL0051	2380	8.462E-15	1.355E-15	12763	2616	20.5
SI5-N	25.7140	XBE0297	0.335	1.0372E-14	6.390E-16	6025	436	7.2	XAL0052	2708	6.489E-15	1.185E-15	12396	3130	25.3
SI5-O	13.8850	XBE0298	0.335	4.631E-15	4.110E-16	4096	538	13.1	XAL0053	2757	2.645E-15	6.235E-16	6336	3859	60.9
SI5-P	30.6980	XBE0299	0.336	7.237E-15	5.937E-16	3296	340	10.3	XAL0054	2414	5.601E-15	1.120E-15	7698	2237	29.1
SI5-S	26.7690	XBE0300	0.337	1.563E-14	7.803E-16	9137	507	5.5	XAL0055	1968	5.625E-15	1.063E-15	7235	2009	27.8
SI5-U	24.7900	XBE0301	0.337	5.116E-15	4.895E-16	2642	354	13.4	XAL0056	2505	4.029E-15	8.793E-16	6347	2411	38.0
SI5-V	15.1400	XBE0302	0.336	3.039E-15	3.231E-16	1981	405	20.4	XAL0057	2751	2.669E-15	7.134E-16	5896	3801	64.5
SI5-X	28.6000	XBE0303	0.335	6.438E-15	4.628E-16	3072	291	9.5	XAL0058	2607	4.994E-15	1.090E-15	7687	2539	33.0
OCS-1	20.1595	BE777	0.8393	3.640E-14	2.108E-15	28644	1687	5.9	AL867	2416	5.805E-14	5.865E-15	152272	15699	10.3
OCS-3	21.0735	BE779	0.8413	3.200E-14	2.683E-15	24084	2059	8.5	AL869	2439	6.931E-14	7.112E-15	176086	18377	10.4
OCS-6	20.1359	BE781	0.8392	3.750E-14	1.941E-15	29571	1555	5.3	AL871	2401	4.511E-14	5.141E-15	117015	13691	11.7
OCS-7	20.0850	BE783	0.8378	3.460E-14	1.531E-15	27272	1228	4.5	AL873	2413	7.134E-14	5.865E-15	188258	15736	8.4
OCS-8	18.5889	BE784	0.8399	3.890E-14	3.141E-15	33196	2728	8.2	AL874	2377	7.287E-14	5.154E-15	204758	14722	7.2
OCS-9	20.3097	BE785	0.8393	8.110E-14	2.421E-15	63933	1923	3.0	AL875	2404	1.123E-13	5.840E-15	293610	15437	5.3
OCS-10	20.1860	BE788	0.8414	2.370E-14	1.007E-15	18515	809	4.4	AL878	2410	6.012E-14	5.233E-15	157154	13953	8.9
OCS-S	20.2644	BE787	0.8311	5.210E-14	2.494E-15	40582	1966	4.8	AL877	2368	1.043E-13	7.150E-15	269108	18655	6.9
OCS-P	16.1230	BE788	0.8354	3.140E-14	1.526E-15	30631	1521	5.0	AL876	2326	6.453E-14	7.307E-15	204129	23538	11.5
SGR-3	22.4709	b7760	0.6975	2.47E-14	1.158E-15	14400	786	5.5	a1899	2141	4.915E-14	2.784E-15	103515	5940	5.7
SGR-1	16.6775	b7770	0.6995	7.90E-14	2.101E-15	67799	1890	2.8	a1909	1991	1.525E-14	6.151E-15	486514	16397	3.4
SGR-2	19.2885	b7772	0.6984	6.98E-15	6.166E-16	3115	521	16.7	a1911	1690	1.673E-13	2.234E-15	32055	4390	13.7

a: Samples SGC2 and STL used an in-house produced Be carrier with a Be concentration of 318 µg g^{-1}. Samples SVF and SCQ used an in-house produced Be carrier with a Be concentration of 204 µg g^{-1}. Samples HCR, SLC, and OCS used an in-house produced Be carrier with a Be concentration of 288 µg g^{-1}. Sample SI5 used an in-house Be carrier with a Be concentration of 758 µg g^{-1}.

b: Be ratios normalized to standards of Nishiizumi et al., (2007).

c: All uncertainties are 1σ confidence level.

d: ^{10}Be concentrations and associated measurement uncertainties for samples were blank corrected using either the batch-specific blank for isochron samples processed in one batch or the average value of multiple blanks if the isochron samples were processed in multiple batches. All blank corrections used blanks measured in the same AMS run as the samples. Average total atoms ^{10}Be in process blanks (errors are 1 σ): HCR = 9510 +/- 2639, SLC and OCS = 9970 +/- 1180, SI5 = 22489 +/- 2725, SVF and SCQ = 27114 +/- 3906, SGC2 = 46366 +/- 7425, STL and SGR = 43510 +/- 6751

e: Propagated uncertainties include 1σ error in AMS measurements, error in the blank, and carrier mass (1%).

f: Al ratios normalized to standards of Nishiizumi et al. (2004).

g: ^{26}Al concentrations and associated measurement uncertainties for samples were blank corrected using either the batch-specific blank for isochron samples processed in one batch or the average value of multiple blanks if the isochron samples were processed in multiple batches. All blank corrections used blanks measured in the same AMS run as the samples. Average total atoms ^{26}Al in process blanks: HCR = 72074 +/- 41618, SLC and OCS = 62722 +/- 11600, SI5 = 72572 +/- 36293, SVF and SCQ = 36414 +/- 21028, SGC2 = 27755 +/- 19627, STL and SGR = 20263 +/- 16269.

Table S3. Sample parameters for the surface exposure dating samples from the Bear Canyon surface

Sample ID	*Cathode Number*	*Location* [a]		*Elevation above Sea Level (m)*	*Thickness (cm)*	*Shielding Factor* [b]	*Boulder Height (m)*	*Quartz (g)*	*Be Carrier* [c] *(g)*	*Standard*	*Measured $^{10}Be/^{9}Be$* [d,e]			*^{10}Be Concentration (atoms g^{-1} SiO_2)* [f,g]			*Model Age (yrs)* [e,h,i]		
		°N	°W																
BCB-1	BE800	34.44493	-119.1145	622	4	0.995	1.6	2.0931	0.8088	07KNSTD	4.490E-14	+/-	1.729E-15	325944	+/-	13171	55332	+/-	3107
BCB-3B	BE765	34.44451	-119.1143	619	3	0.976	2.0	6.6529	0.8407	07KNSTD	1.611E-13	+/-	4.260E-15	387155	+/-	11007	66839	+/-	3219
BCB-5	BE766	34.44271	-119.1127	606	4	0.997	2.2	7.0463	0.8409	07KNSTD	1.630E-13	+/-	4.310E-15	372036	+/-	10575	63953	+/-	3078
BCB-7	BE767	34.44148	-119.1118	604	4	0.989	2.4	7.5634	0.8421	07KNSTD	2.731E-13	+/-	7.700E-15	584101	+/-	17526	102334	+/-	5074
BCB-8	BE768	34.44140	-119.1118	604	7	0.996	1.3	7.4074	0.8387	07KNSTD	3.113E-13	+/-	8.769E-15	676762	+/-	20282	120903	+/-	6020
BCB-9	BE770	34.44353	-119.1124	610	6	0.997	1.6	8.9269	0.8390	07KNSTD	1.017E-13	+/-	2.933E-15	181156	+/-	5589	31245	+/-	1538
BCB-10	BE771	34.44361	-119.1124	612	7	0.988	2.6	7.5474	0.8374	07KNSTD	1.072E-13	+/-	3.323E-15	225948	+/-	7431	39628	+/-	2008
BCB-13	BE772	34.44484	-119.1135	621	3	0.998	2.2	7.0039	0.8391	07KNSTD	2.963E-13	+/-	7.714E-15	681441	+/-	19062	116332	+/-	5640
BCB-14	BE773	34.44470	-119.1140	618	7	0.998	3.9	6.6030	0.8382	07KNSTD	1.833E-13	+/-	4.833E-15	445125	+/-	12619	77672	+/-	3747
BCB-15	BE774	34.44581	-119.1141	627	5	0.990	2.0	6.1815	0.8355	07KNSTD	2.835E-13	+/-	7.558E-15	733279	+/-	20945	127806	+/-	6261

a: Coordinates are in WGS84.

b: Calculated using the CRONUS-Earth Geometric Shielding Calculator version 1.1 (available online at: http://hess.ess.washington.edu/).

c: In-house produced Be carrier has a Be concentration of 288 µg g^{-1}.

d: AMS measured ratios were normalized to standard 01-5-2 with an assumed $^{10}Be/^{9}Be$ ratio of 8.558 x 10^{-12} (Nishiizumi et al., 2007).

e: Uncertainties for all concentrations and ages are 1 σ confidence level.

f: ^{10}Be concentrations and associated measurement uncertainties are blank corrected relative to batch specific process blanks. Total atoms ^{10}Be in process blanks: BCB-1 = 10701 +/- 3102, all other samples = 12107 +/- 4037.

g: Propagated uncertainties include the error in the blank, carrier mass (1%), and sample.

h: Age calculated using version 3.0 of the CRONUS-Earth online exposure age calculator (available online at: https://hess.ess.washington.edu/).

i: Constant (time-invariant) scaling scheme of Lal (1991) and Stone (2000) with a reference production rate of 4.24 +/- 0.16 atoms g^{-1} yr^{-1} based on Promontory Point (PPT) calibration data from Lifton et al., (2015).

All ages assume an erosion rate of 0 mm yr^{-1}.

Table S4. Parameters for ^{10}Be erosion rate samples and inputs to CRONUS calculator

Catchment	*Sample ID*	*Cathode Number*	*Latitude (°N)* [a]	*Longitude (°W)* [a]	*Elevation (m.a.s.l)* [b]	*Quartz Mass (g)*	*Be Carrier (g)* [c]	*Measured ^{10}Be/^{9}Be* [d]	*^{10}Be Concentration (atoms g^{-1} SiO$_2$)* [e]	*Effective Latitude (°N)* [i]	*Effective Longitude (°W)* [i]	*Effective Elevation (m)* [i]	*Av. Topographic Shielding* [f]	*Erosion rate (mm yr^{-1})* [g]	*^{10}Be Erosional Timescale (years)* [h]
1	SCT	BE45101	34.46800	-119.17200	453	9.14	0.3374	1.14E-14 +/- 6.79E-16	17906 +/- 1356	34.4876	-119.1615	1121	0.979	0.33 +/- 0.04	2410
3	SCS	BE45099	34.44366	-119.13450	521	16.58	0.3375	1.22E-13 +/- 2.46E-15	123983 +/- 2554	34.4791	-119.1232	1224	0.969	0.05 +/- 0.01	16000
4	SCB	BE45100	34.44136	-119.12214	506	17.49	0.3371	2.58E-14 +/- 9.36E-16	23440 +/- 948	34.4610	-119.1108	962	0.963	0.23 +/- 0.02	3524
5	SCSP	BE45095	34.43133	-119.09092	175	17.75	0.3375	4.65E-15 +/- 4.22E-16	2724 +/- 474	34.4685	-119.0634	1197	0.968	2.30 +/- 0.39	348
8	SCP	BE45096	34.41244	-118.89864	209	9.74	0.3365	4.30E-15 +/- 4.68E-16	4336 +/- 932	34.4382	-118.8830	682	0.967	1.04 +/- 0.21	769
9	SCH	BE45097	34.41669	-118.83309	209	16.94	0.3374	6.20E-15 +/- 4.91E-16	4418 +/- 558	34.4683	-118.8386	814	0.975	1.12 +/- 0.15	714
10	SCM	BE45098	34.42757	-118.77036	255	17.40	0.3396	5.46E-15 +/- 4.83E-16	3601 +/- 540	34.4391	-118.7868	532	0.963	1.14 +/- 0.18	702
11	SSCB	BE45094	34.41200	-118.97500	270	16.75	0.3363	1.15E-14 +/- 7.12E-16	9838 +/- 769	34.4302	-118.9893	904	0.963	0.52 +/- 0.06	1572
13	SSCO	BE45093	34.37748	-119.04046	139	18.10	0.3371	1.58E-14 +/- 1.04E-15	13208 +/- 1014	34.4020	-119.0366	538	0.988	0.31 +/- 0.03	2548
14	SSCM	BE45092	34.40111	-119.07000	225	16.20	0.3327	5.64E-15 +/- 5.07E-16	3972 +/- 590	34.4161	-119.0504	662	0.980	1.14 +/- 0.18	702
17	SSCOH	BE45091	34.34894	-119.11119	102	18.89	0.3363	2.03E-14 +/- 9.24E-16	16706 +/- 865	34.3656	-119.1244	230	0.992	0.20 +/- 0.02	3941
18	VTW	BE45090	34.33776	-119.14217	113	15.92	0.3368	1.16E-14 +/- 1.05E-15	10444 +/- 1160	34.3772	-119.1476	331	0.989	0.35 +/- 0.05	2292
19	VTA	BE45089	34.3176	-119.14462	99	18.18	0.3352	1.18E-14 +/- 9.66E-16	9287 +/- 934	34.3704	-119.1799	350	0.989	0.40 +/- 0.05	2010
20	VTPT	BE45088	34.31034	-119.15312	90	18.18	0.3355	2.32E-14 +/- 1.27E-15	19995 +/- 1210	34.3277	-19.1733	250	0.993	0.17 +/- 0.02	4819
23	VTHA	BE45087	34.28601	-119.25642	63	19.16	0.3356	1.00E-14 +/- 7.49E-16	10430 +/- 702	34.3145	-119.2483	237	0.982	0.33 +/- 0.03	2454
24	VTCL	BE45084	34.34259	-119.28571	75	17.57	0.3349	9.42E-15 +/- 5.75E-16	7172 +/- 607	34.3703	-119.2399	341	0.986	0.51 +/- 0.06	1566
25	VTCDA	BE45085	34.35331	-119.26002	133	16.86	0.3467	1.17E-14 +/- 7.17E-16	10257 +/- 793	34.3700	-119.267	275	0.986	0.34 +/- 0.04	2339

a: Coordinates are in WGS84

b: m.a.s.l = Meters above sea level.

c: In-house produced Be carrier has a Be concentration of 758 µg g^{-1}.

d: AMS measured ratios were normalized to standard 01-5-2 with an assumed ^{10}Be/^{9}Be ratio of 8.558 x 10^{-12} (Nishiizumi et al., 2007). All uncertainties are 1σ confidence level.

e: ^{10}Be concentrations and associated measurement uncertainties are blank corrected relative to the average of the two blanks processed alongside the samples in the laboratory. Total atoms ^{10}Be in process blanks: Catchments 1-13 = 31126 +/- 4227, catchment 14-25 = 30933 +/- 4391, average value = 31029 +/– 136 atoms. All uncertainties are external uncertainties and are 1σ confidence level.

f: Topographic shielding calculated using algorithms in Mudd et al., (2016).

g: Calculated using the CRONUS online calculator version 3 (available at: https://hess.ess.washington.edu; Balco et al., [2008]). Calculations used a density of 2.65 g cm^{-3}, thickness of 1 cm, Be standardization 07KNSTD from Nishiizumi et al., (2007), and the constant production rate model of Lal (1991) and Stone (2000).

h: Time required to remove one mean attenuation path length, T=z∗/e, using z∗ = 80 cm (typical for silicate rocks; Yanites et al., 2009) and e=erosion rate.

i: Latitude, longitude, and elevation that correspond to the hypsometry-weighted production rate for the catchment.

Table S5. Well data for wells used in cross section in Figure 6B

Well ID	*API*	*Lease Name*	*Section*	*Township*	*Range*
1	11120083	Dankar-Alpert	35	03N	30W
2	11105866	Berywood Investment Company	36	03N	20W
3	11105864	Johnson	24	03N	20W
4	11121015	Glad	18	03N	19W
5	11100452	Geis-Robertson	12	03N	20W
6	11106071	Kenneth H. Hunter-River Ranch	36	04N	20W

Well data collected from the California Department of Conservation: Well Finder. Available at: www.maps.conservation.ca.gov [last accessed: 09/09/2020]

Table S6. Alternative isochron burial ages

Isochron	Preferred Slope	Preferred Intercept (^{26}Al atoms/g)	Preferred Post Burial Production ^{26}Al Concentration*	Preferred Age (Ma)	Alternative Slope	Alternative Age (Ma)**	Notes
Base Las Posas, Ventura (HCR)	$5.05^{+0.15}/_{-0.13}$	$462^{+1402}/_{-462}$	4 % (1 %)	$0.60^{+0.05}/_{-0.06}$	$5.19^{+0.42}/_{-0.35}$	$0.55^{+0.15}/_{-0.16}$	*Alternative age without the highest concentration sample (HCR-6) overlaps with preferred age when sample HCR-6 is included. Sample HCR-2 (nuclide concentration reset by post-burial production) is also omitted from all ages.*
Top Saugus, Ventura (SVF)	$5.66^{+0.62}/_{-0.48}$	$5996^{+3540}/_{-4782}$	24 % (12 %)	$0.36^{+0.18}/_{-0.22}$	$6.66^{+0.07}/_{-1.12}$	*Indistinguishable from the surface production ratio*	*Alternative slope when sand sample omitted is indistinguishable from the surface production ratio. Samples SVF-B (complex burial history) and SVF-C (nuclide concentration reset by post-burial production) are also omitted from preferred age.*
					5.30 +/- 1.16	*0.50 +/- 0.46*	*Removing just SVF-B*
					5.61 +/- 1.54	*$0.38^{+0.56}/_{-0.58}$*	*Removing just SVF-C*
Base GCDF, Oak Ridge (SGC2)	$4.05^{+0.25}/_{-0.22}$	$4288^{+2878}/_{-3255}$	21 % (7 %)	1.06 +/- 0.12	NA	NA	*No alternative age.*
Top Saugus, Happy Camp Syncline (SCQ)	$4.21^{+0.61}/_{-0.39}$	$24331^{+6231}/_{-7945}$	34 % (27 %)	$0.98^{+0.20}/_{-0.28}$	*3.10 +/- 1.42*	*$1.61^{+0.96}/_{-0.98}$*	*Alternative age includes sand sample.*
Top Saugus, Long Canyon Syncline (SLC)	$4.04^{+0.54}/_{-0.42}$	$37809^{+11634}/_{-14868}$	32 % (25 %)	$1.06^{+0.23}/_{-0.26}$	$3.88^{+0.51}/_{-0.39}$	$1.15^{+0.22}/_{-0.26}$	*Alternative age includes sand sample. SLC-Peb is also omitted from all ages.*
Base Sunshine Ranch, East Ventura Basin (SI5)	$1.37^{+0.30}/_{-0.19}$	$2807^{+816}/_{-1286}$	44 % (33 %)	$3.30^{+0.30}/_{-0.41}$	*$0.38^{+0.62}/_{-0.38}$*	*$5.97^{+3.44}/_{-3.50}$*	*Alternative age includes sand sample.*
Top Saugus, East Ventura Basin (STL)	$4.52^{+1.00}/_{-0.72}$	$4084^{+7182}/_{-4084}$	11 % (7 %)	$0.83^{+0.36}/_{-0.41}$	*2.33 +/- 1.66*	*$2.20^{+1.46}/_{-1.48}$*	*Alternative age includes sand sample but excludes sample STL-3 (nuclide concentration reset by post-burial production).*
					$1.86^{+0.29}/_{-0.20}$	$2.66^{+0.24}/_{-0.30}$	*Alternative age includes sand sample but excludes STL-5 and STL-3 (nuclide concentration reset by post-burial production).*

Note: NA = Not applicable

** Percentage of post-burial production relative to the concentration of the lowest ^{26}Al concentration sample. Percentage in parentheses is post-burial production relative to the mean ^{26}Al concentration.*

*** Non-italicized slopes and ages are most likely (modal) values from Bayesian analysis with 95 % confidence limits. Alternative slopes and ages in italics returned no results from a Bayesian analysis and the burial age is estimated using the slope derived from a York regression (York, 1966). Uncertainties for alternative ages and slopes are 2σ.*

Table S7. Details on process blanks for Be analysis

Sample	*Cathode Number*	*Be Carrier [b] (g)*	*$^{10}Be/^{9}Be$ [c,d]*			*^{10}Be Atoms [d]*		
Isochron Burial Samples								
B534D	b7754	0.6979	3.125E-15	+/-	4.99E-16	46366	+/-	7425
B535E	b7771	0.6999	2.731E-15	+/-	4.07E-16	40645	+/-	6075
B595H	BE723	0.8382	5.560E-16	+/-	1.31E-16	9192	+/-	2169
B597I	BE736	0.8390	6.937E-16	+/-	1.48E-16	11184	+/-	2387
B603A	BE776	0.8410	1.765E-15	+/-	3.46E-16	28527	+/-	5602
B605B	BE789	0.8425	5.875E-16	+/-	1.63E-16	9510	+/-	2639
SI5 BLK	XBE0294	0.8424	1.286E-15	+/-	1.55E-16	22489	+/-	2726
CFG1401	BE37796	1.0061	1.977E-15	+/-	2.84E-16	27114	+/-	3906
Catchment-Averaged Erosion Rates								
BLK110418	BE45102	0.3372	1.827E-15	+/-	2.59E-16	30933	+/-	4391
BLK160418	BE45103	0.3338	1.820E-15	+/-	2.47E-16	31126	+/-	4227
Exposure Dating Samples								
B602L	BE775	0.8346	7.501E-16	+/-	2.50E-16	12107	+/-	4037
B606C	BE802	0.8359	6.620E-16	+/-	1.92E-16	10701	+/-	3102

a: bXXX = measured at SUERC; BEXXX and XBEXXXX = measured at ANSTO, BEXXXXX = measured at Lawrence Livermore National Laboratory.
b: Sample CFG1401 used an in-house produced Be carrier with a Be concentration of 204 µg g^{-1}. Samples B534D and B535E used an in-house produced Be carrier with a Be concentration of 318 µg g^{-1}. Samples B595H, B597I, B602L, B603C, B605B, and B606C used an in-house produced Be carrier with a Be concentration of 288 µg g^{-1}. Sample SI5 BLK, BLK110418, and BLK160418 used an in-house Be carrier with a Be concentration of 758 µg g^{-1}.
c: Be ratios normalized to standards of Nishiizumi et al., (2007).
d: All uncertainties are 1σ confidence level.

Table S8. Details on process blanks for Al analysis

Sample	*Cathode Number [a]*	*Total Al (µg)*	*$^{26}Al/^{27}Al$ [b,c]*			*^{26}Al Atoms [c]*		
B534D	a1893	1972	6.306E-16	+/-	4.459E-16	27755	+/-	19627
B535E	a1910	1938	3.065E-16	+/-	3.065E-16	13254	+/-	13253
B595H	AL854	2603	1.312E-15	+/-	5.868E-16	76213	+/-	34095
B597I	AL865	2436	9.737E-16	+/-	6.885E-16	52948	+/-	37443
B603A	AL866	2437	9.271E-16	+/-	9.271E-16	50434	+/-	50437
B605B	AL879	2464	1.310E-15	+/-	7.565E-16	72074	+/-	41618
SI5 BLK	XAL0049	2675	1.215E-15	+/-	6.077E-16	72572	+/-	36293
CFG1401	a2058	1954	8.352E-16	+/-	4.822E-16	36414	+/-	21028

a: aXXX = measured at SUERC; ALXXX and XALXXXX = measured at ANSTO
b: Al ratios normalized to standards that are consistent with values of Nishiizumi et al., (2004). See Supplemental Materials text for more details on standards used at SUERC versus ANSTO.
c: All uncertainties are 1σ confidence level.

Table S9. Be details for CRONUS-N samples

Sample	*Cathode Number* [a]	*Quartz (g)*	*Be Carrier* [b] *(g)*	*$^{10}Be/^{9}Be$* [c,d]			*^{10}Be Atoms* [d]		
Isochron burial dating samples									
B534K	b7764	10.1131	0.6978	1.384E-13	+/-	6.054E-15	198450	+/-	8911
B535L	b7780	10.6100	0.6979	1.635E-13	+/-	2.902E-15	224836	+/-	4098
B595B	BE717	10.0263	0.8399	1.405E-13	+/-	3.900E-15	231210	+/-	6447
B597C	BE730	11.1156	0.8378	1.755E-13	+/-	4.591E-15	253156	+/-	6652
B603G	BE782	11.3741	0.8371	1.759E-13	+/-	5.293E-15	247876	+/-	7488
B605H	BE795	11.1349	0.8370	1.634E-13	+/-	4.282E-15	235153	+/-	6189
Surface exposure dating samples									
B602F	BE769	11.0196	0.8399	1.566E-13	+/-	6.214E-15	228240	+/-	9108

a: bXXX = measured at SUERC; BEXXX = measured at ANSTO

b: Samples B534K and B535L used an in-house produced Be carrier with a Be concentration of 318 µg g^{-1}. Samples B595B, B597C, B602F, B603G, and B605H used an in-house produced Be carrier with a Be concentration of 288 µg g^{-1}.

c: Be ratios normalized to standards of Nishiizumi et al., (2007).

d: All uncertainties are 1σ confidence level.

Table S10. Al details for CRONUS-N samples

Sample	*Cathode Number* [a]	*Quartz (g)*	*Total Al (µg)*	*$^{26}Al/^{27}Al$* [b,c]			*^{26}Al Atoms* [c]		
B534K	a1903	10.1131	2660	1.673E-13	+/-	6.167E-15	978424	+/-	36298
B535L	a1919	10.6100	2700	1.848E-13	+/-	5.676E-15	1047861	+/-	32285
B595B	AL848	10.0263	3488	1.221E-13	+/-	4.809E-15	937850	+/-	37616
B597C	AL861	11.1156	3867	1.326E-13	+/-	6.435E-15	1022017	+/-	50250
B603G	AL872	11.3741	4743	1.162E-13	+/-	1.180E-14	1072846	+/-	110161
B605H	AL885	11.1349	3833	1.470E-13	+/-	1.084E-14	1119323	+/-	83485

a: aXXX = measured at SUERC; ALXXX = measured at ANSTO

b: Al ratios normalized to standards that are consistent with values of Nishiizumi et al., (2004). See Supplemental Materials text for more details on standards used at SUERC versus ANSTO.

c: All uncertainties are 1σ confidence level.